

First Census of Sub-kiloparsec Resolution Metallicity Gradients in Star-forming Galaxies at Cosmic Noon from *HST* Slitless Spectroscopy

XIN WANG,^{1,2} TUCKER A. JONES,³ TOMMASO TREU,² EMANUELE DADDI,⁴ GABRIEL B. BRAMMER,⁵ KEREN SHARON,⁶ TAKAHIRO MORISHITA,⁷
LOUIS E. ABRAMSON,⁸ JAMES W. COLBERT,¹ ALAINA L. HENRY,⁷ PHILIP F. HOPKINS,⁹ MATTHEW A. MALKAN,² KASPER B. SCHMIDT,¹⁰
HARRY I. TEPLITZ,¹ AND BENEDETTA VULCANI¹¹

¹*Infrared Processing and Analysis Center, Caltech, 1200 E. California Blvd., Pasadena, CA 91125, USA*

²*Department of Physics and Astronomy, University of California, Los Angeles, CA 90095-1547, USA*

³*University of California Davis, 1 Shields Avenue, Davis, CA 95616, USA*

⁴*Laboratoire AIM, CEA/DSM-CNRS-Université Paris Diderot, IRFU/Service d'Astrophysique, Bât. 709, CEA Saclay, F-91191 Gif-sur-Yvette Cedex, France*

⁵*Cosmic Dawn Centre, University of Copenhagen, Blegdamsvej 17, 2100 Copenhagen, Denmark*

⁶*Department of Astronomy, University of Michigan, 1085 S. University Avenue, Ann Arbor, MI 48109, USA*

⁷*Space Telescope Science Institute, 3700 San Martin Drive, Baltimore, MD, 21218, USA*

⁸*The Observatories of the Carnegie Institution for Science, 813 Santa Barbara St., Pasadena, CA 91101, USA*

⁹*TAPIR, California Institute of Technology, Pasadena, CA 91125, USA*

¹⁰*Leibniz-Institut für Astrophysik Potsdam (AIP), An der Sternwarte 16, D-14482 Potsdam, Germany*

¹¹*INAF- Osservatorio Astronomico di Padova, Vicolo Osservatorio 5, I-35122 Padova, Italy 0000-0003-0980-1499*

Abstract

We present hitherto the largest sample of gas-phase metallicity radial gradients measured at sub-kiloparsec resolution in star-forming galaxies in the redshift range of $z \in [1.2, 2.3]$. These measurements are enabled by the synergy of slitless spectroscopy from the Hubble Space Telescope near-infrared channels and the lensing magnification from foreground galaxy clusters. Our sample consists of 79 galaxies with stellar mass ranging from 10^7 to $10^{10} M_{\odot}$, instantaneous star-formation rate in the range of $[1, 100] M_{\odot}/\text{yr}$, and global metallicity $[\frac{1}{12}, 2]$ solar. At $2\text{-}\sigma$ confidence level, 14/79 galaxies in our sample show negative radial gradients, whereas 7/79 show inverted gradients. Combining ours and all other metallicity gradients obtained at similar resolution currently available in the literature, we measure a negative mass dependence of $\Delta \log(\text{O}/\text{H})/\Delta r$ [dex kpc^{-1}] = $(-0.020 \pm 0.007) + (-0.014 \pm 0.008) \log(M_*/10^{9.4} M_{\odot})$ with the intrinsic scatter being $\sigma = 0.060 \pm 0.006$ over four orders of magnitude in stellar mass. Our result is consistent with strong feedback, not secular processes, being the primary governor of the chemo-structural evolution of star-forming galaxies during the disk mass assembly at cosmic noon. We also find that the intrinsic scatter of metallicity gradients increases with decreasing stellar mass and increasing specific star-formation rate. This increase in the intrinsic scatter is likely caused by the combined effect of cold-mode gas accretion and merger-induced starbursts, with the latter more predominant in the dwarf mass regime of $M_* \lesssim 10^9 M_{\odot}$.

Keywords: galaxies: abundances — galaxies: evolution — galaxies: formation — galaxies: high-redshift — gravitational lensing: strong

1. INTRODUCTION

Metallicity is one of the most fundamental proxies of galaxy evolution at the peak of cosmic star formation and metal enrichment ($1 \lesssim z \lesssim 3$), i.e., the cosmic noon epoch (Madau & Dickinson 2014). The interstellar medium oxy-

gen abundance relative to hydrogen — metallicity¹ — has been shown to correlate strongly with stellar mass (M_*), star-formation rate (SFR) and gas fraction (see the recent review by Maiolino & Mannucci 2018, and references therein). The cumulative history of the baryonic mass assembly, e.g., star formation, gas accretion, mergers, feedback and galactic winds, altogether governs the total amount of metals remain-

Corresponding author: Xin Wang
wangxin@ipac.caltech.edu

¹ Throughout this paper, we use metallicity to stand for gas-phase oxygen abundance unless otherwise specified.

ing in gas (Finlator & Davé 2008; Davé et al. 2012; Lilly et al. 2013; Dekel & Mandelker 2014; Peng & Maiolino 2014). Moreover, these baryon cycling processes also tightly regulate the spatial distribution of metals in galaxies. Thus, a powerful way to learn about the baryon cycle is to use spatially resolved information.

The conventional way to obtain spatially resolved information is through integral field spectroscopy (IFS). IFS has dramatically expanded our vision of galaxies from spectroscopic measurements integrated through single slits/fibres to panoramic 2-dimensional (2D) views across their full surfaces, allowing for spatial variations of physical properties (including metallicity). This facilitates several large ground-based surveys (e.g. CALIFA, MaNGA, SAMI) to constrain the radial profile of metallicity in hundreds of galaxies, successfully capturing the dynamic signatures of the baryon cycle (see e.g., Sanchez et al. 2014; Belfiore et al. 2017; Poteirojo et al. 2018). Meanwhile numerical simulations are now capable of making useful predictions for metallicity radial gradients and their evolution with redshift (e.g. Ma et al. 2017; Tissera et al. 2018). The main challenge for observations is that sub-kiloparsec (sub-kpc) spatial resolution is required for accurate results and meaningful comparison with theoretical predictions. While this spatial sampling is readily achieved for nearby galaxies ($z \lesssim 0.3$), seeing-limited data are insufficient for galaxies at moderate to high redshift. Therefore we need an effective approach to achieve sub-kpc resolved spectroscopy for statistically representative samples of high- z galaxies to compare meaningfully with cosmological zoom-in simulations.

The approach we take is space-based slitless spectroscopy. Building upon our previous efforts (Jones et al. 2015; Wang et al. 2017, 2019), we exploit grism spectroscopy from the Hubble Space Telescope (*HST*). *HST*'s diffraction limit in near-infrared (NIR) is equivalent to a physical scale of ~ 1 kpc at $z \sim 2$. Additional gain in resolution can be provided by gravitational lensing by foreground galaxies and/or galaxy clusters to fully satisfy the requirement for sufficiently resolving the chemical profiles of galaxies at that epoch. Lensing is thus essential for resolving the lowest-mass galaxies at high redshifts. In this work, we measure radial gradients of metallicity in 79 star-forming galaxies at $1.2 \lesssim z \lesssim 2.3$ gravitationally lensed by foreground galaxy clusters. Our sample presents a clear step forward in the comparison between observed and simulated chemo-structural properties of galaxies, offering tremendous insights into galaxy evolution.

This paper is organized as follows. In Section 2, we describe the data and galaxy sample analyzed in this work. The measurements of various physical quantities for our sample galaxies are presented in Section 3. Then two major pieces of our analysis results, i.e., the redshift evolution and mass dependence of sub-kpc resolution metallic-

ity gradients, are shown in Sections 4 and 5, respectively. We finally conclude in Section 6. Throughout this paper, the AB magnitude system and standard concordance cosmology ($\Omega_m = 0.3$, $\Omega_\Lambda = 0.7$, $H_0 = 70 \text{ km s}^{-1} \text{ Mpc}^{-1}$) are used. Forbidden lines are indicated as follows: [O III] $\lambda 5008 :=$ [O III], [O II] $\lambda \lambda 3727, 3730 :=$ [O II], [N II] $\lambda 6585 :=$ [N II], [S II] $\lambda \lambda 6718, 6732 :=$ [S II], if presented without wavelength values.

2. DATA AND SAMPLE SELECTION

The spectroscopic data analyzed in this work are acquired by the Grism Lens-Amplified Survey from Space² (*GLASS*; Proposal ID 13459; P.I. Treu, Schmidt et al. 2014; Treu et al. 2015). It is a cycle-21 *HST* large program allocated 140 orbits of Wide-Field Camera 3 (WFC3) NIR slitless spectroscopy on the centers of 10 strong-lensing galaxy clusters. For each cluster center field, we have 10 orbits of G102 (covering $0.8\text{--}1.15 \mu\text{m}$) and 4 orbits of G141 (covering $1.1\text{--}1.7 \mu\text{m}$) exposures, amounting to ~ 22 kilo-seconds of G102 and ~ 9 kilo-seconds of G141 in total, together with ~ 7 kilo-seconds of F105W+F140W direct imaging for wavelength/flux calibration and astrometric alignment. This exposure time is divided equally into two orients with almost orthogonal light dispersion directions, designed to disentangle contamination from neighbor objects. As a result, we obtain two suites of G102+G141 spectra for each object, in an uninterrupted wavelength range of $0.8\text{--}1.7 \mu\text{m}$ with nearly uniform sensitivity, reaching $1\text{-}\sigma$ surface brightness of $3 \times 10^{-16} \text{ erg s}^{-1} \text{ cm}^{-2} \text{ arcsec}^{-2}$. The 10 cluster fields are listed in Table 1 and shown in Fig. 1. Among these clusters, 6 have ultra-deep 7-filter imaging from the Hubble Frontier Fields (*HFF*) initiative (Lotz et al. 2016). The other 4 have multi-band imaging from the Cluster Lensing And Supernova survey with Hubble (*CLASH*) (Postman et al. 2012).

We base our source selection on the redshift catalogs made public by the *GLASS* collaboration. From these catalogs, we select ~ 300 galaxies with secure spectroscopic redshifts in the range of $z \in [1.2, 2.3]$. This redshift range is chosen to enable the grism coverage of the oxygen collisionally excited lines and the Balmer lines in rest-frame optical (i.e., [O III], H β , [O II]), which are the most promising and frequently used metallicity diagnostics at extragalactic distances. We also visually inspected the spatial extent and grism data quality of each source, to remove sources with compact morphology and/or severe grism defects, not suitable for our analysis. We end up with around 100 galaxies for subsequent measurements.

3. MEASUREMENTS

² <https://archive.stsci.edu/prepds/glass/>

Table 1. Summary of the *HST* observations presented in this work

Cluster Field	Cluster Alias	Cluster Redshift	R.A.	Decl.	Grism PA ^a	<i>HST</i> imaging	N_{source} ^b
			(deg.)	(deg.)	(deg.)		
Abell 2744	A2744	0.308	00:14:21.2	-30:23:50.1	135, 233	<i>HFF</i>	13
Abell 370	A370	0.375	02:39:52.9	-01:34:36.5	155, 253	<i>HFF</i>	7
MACS0416.1-2403	MACS0416	0.420	04:16:08.9	-24:04:28.7	164, 247	<i>HFF/CLASH</i>	10
MACS0717.5+3745	MACS0717	0.548	07:17:34.0	+37:44:49.0	020, 280	<i>HFF/CLASH</i>	6
MACS0744.9+3927	MACS0744	0.686	07:44:52.8	+39:27:24.0	019, 104	<i>CLASH</i>	6
MACS1423.8+2404	MACS1423	0.545	14:23:48.3	+24:04:47.0	008, 088	<i>CLASH</i>	9
MACS2129.4-0741	MACS2129	0.570	21:29:26.0	-07:41:28.0	050, 328	<i>CLASH</i>	11
RXJ1347.5-1145	RXJ1347	0.451	13:47:30.6	-11:45:10.0	203, 283	<i>CLASH</i>	2
RXJ2248.7-4431	RXJ2248	0.348	22:48:44.4	-44:31:48.5	053, 133	<i>HFF/CLASH</i>	5
MACS1149.6+2223 ^c	MACS1149	0.544	11:49:36.3	+22:23:58.1	032, 111, 119, 125	<i>HFF/CLASH</i>	10

NOTE—Here we only list the primary pointings of the analyzed *HST* slitless spectroscopy, covering the cluster centers with WFC3/NIR grisms.

^aThe position angles (PAs) are represented by the “PA_V3” values reported in the corresponding raw image headers. The PA of the actual dispersion axis of slitless spectroscopy, in degrees east of north, is given by $\text{PA}_{\text{disp}} \approx \text{PA_V3} - 45.2$. For each one of the *GLASS* PAs (i.e. excluding PAs 111 and 119 for MACS1149), 2 orbits of G141 and 5 orbits of G102 exposures have been taken, amounting to ~ 4.5 and ~ 11 kilo-seconds science exposure times for G141 and G102 respectively.

^bThe number of galaxies in which we secure sub-kpc resolution metallicity gradient measurements from *HST* spectroscopy.

^cThe detailed analyses of gradient measurements have already been presented in our earlier paper (Wang et al. 2017). Here we update the SED fitting results associated with these galaxies.

3.1. Emission line flux

We adopt the Grism Redshift and Line Analysis software (GRIZLI³; G. Brammer et al. in prep) to handle wide-field slitless spectroscopy data reduction. GRIZLI is a state-of-the-art software that performs “one-stop-shopping” processing of paired direct and grism exposures acquired by space telescopes. The entire procedure consists of five steps: 1) pre-processing of raw grism exposures⁴, 2) forward modeling full field-of-view (FoV) grism images, 3) redshift fitting via spectral template synthesis, 4) refining full FoV grism model, and 5) extracting 1D/2D spectra and emission line (EL) maps of individual targets.

In Step 3), we derive the best-fit redshift of our sources from spectral template fitting based on a library of spectral energy distributions (SED) of stellar populations with a range of characteristic ages (see Appendix A in Wang et al. 2019, for more details). We also fit the intrinsic nebular emission using 1D Gaussian functions centered at corresponding

wavelengths and estimate the line fluxes. The morphological broadening is taken into account with respect to the dispersion direction associated with each exposure. Owing to the source selection technique and sensitive grism instruments, the majority of our galaxies show ≥ 5 signal-to-noise ratio (SNR) detections of [O III], H β , H γ and [O II]. For galaxies at $z \leq 1.6$, we also typically have access to their H α and [S II], which help constrain metallicity and nebular extinction. The best-fit redshifts and observed EL fluxes for our sources are presented in Table 3.

3.2. Emission line map

In addition to the measurements of integrated EL fluxes, another key piece of information that we need to retrieve from grism spectroscopy is the spatial distribution of EL surface brightnesses, i.e., the EL maps. The *HST* WFC3/NIR grisms have limited spectral resolution: for point sources, $R \sim 210$ and 130, for G102 and G141, respectively. Yet this is actually an advantage in obtaining EL maps. Since the instrument full-width half-maximum (FWHM) is equivalently ~ 700 km/s for G102, and ~ 1200 km/s for G141, it is reasonable to assume that the source 1D spectral shapes and 2D EL maps are not affected by any kinematic motions of gas ionized by the star-forming regions, where outflows typically have speed < 500 km/s (see e.g. Erb 2015, for a recent re-

³ <https://github.com/gbrammer/grizli/>

⁴ Specifically, step 1) includes bad-pixel/persistence masking, dark/bias subtraction, cosmic ray flagging, overscan correction, relative/absolute astrometric alignment, flat fielding, master/variable sky background subtraction, geometric distortion correction, extraction of source catalogs and segmentation images at visit levels.

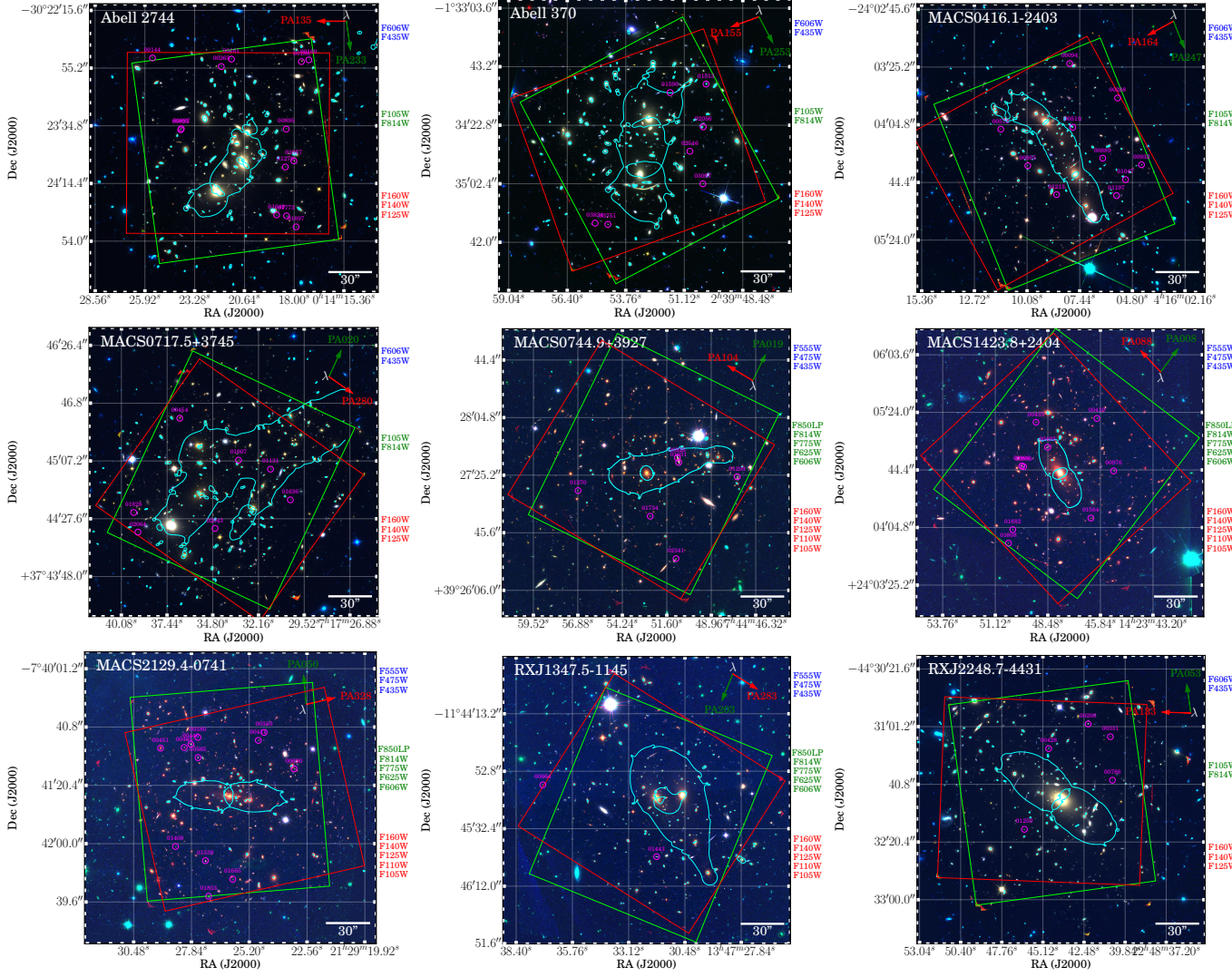


Figure 1. Color-composite images of the nine cluster center fields presented in this work (for the tenth field, i.e., MACS1149, see Fig. 1 of Wang et al. (2017)). The blue, green and red channels are stacked images from the *HFF/CLASH* mosaics taken at various filters, shown on the right to each panel. The footprints of *HST* WFC3/NIR grism pointings are denoted by the red and green squares, with the corresponding wavelength dispersion directions marked by the arrows in the same color in the upper right corner. The cyan contours represent the critical curves at sample median redshift ($z = 1.63$) predicted by our default macroscopic lens models (see Sect. 3.6). Our sources with sub-kpc resolution metallicity gradient measurements are marked by magenta circles.

view). However, as our sample galaxies are selected to be spatially extended, their spatial profiles along the light dispersion direction are convolved onto the wavelength axis, resulting in severe morphological broadening of the line-spread function FWHM (van Dokkum et al. 2011). This morphological broadening effect is already taken into account when estimating the best-fit grism redshift from the spectral template synthesis process described in Sect. 3.1. It also poses a great challenge for obtaining spatial 2D maps of ELs that have very close rest-frame wavelengths, in particular the line complex of $H\beta + [O III] \lambda\lambda 4960, 5008$ doublets.

We hence develop a custom technique to deblend the line complex as follows. First, we measure the source broad-band

isophotes that encompass over 90% of the surface brightness in JH_{140} and Y_{105} -band, and overlay them on top of the source 2D G141 and G102 spectra respectively. The 2D grism spectra are standard data products produced by our GRIZLI reduction with contamination and source continuum removed. The positions of the overlaid isophotes on the 2D grism spectra mark the locations of the redshifted ELs (see the middle and bottom rows of Fig. 2). We rely on the pre-imaging (i.e. JH_{140} and Y_{105}) paired with the grism (i.e. G141 and G102) observations to measure the isophotes because they cover similar wavelength range, share comparable PSF properties, and are acquired at the same PA of the telescope. In this step, the grism spectra taken

at different PAs have to be processed separately, since the morphological broadening varies drastically amongst different PAs if the source has asymmetric radial profiles. This broad-band isophote is used as an aperture for EL map extraction. Since the red (i.e. more to the right on the wavelength axis in 2D spectra) portion of the aperture centered at the redshifted [O III] $\lambda 5008$ is not contaminated by [O III] $\lambda 4960$ and the flux ratio between the [O III] doublets is fixed ($f_{[\text{O III}] 5008}/f_{[\text{O III}] 4960} = 2.98:1$, calculated by Storey & Zeippen (2000)), we can obtain the same red portion of the clean [O III] $\lambda 4960$ 2D map. This red part of [O III] $\lambda 4960$ map is contaminating slightly bluer part of the [O III] $\lambda 5008$ map, and can be subtracted off, with flux errors properly propagated, therefore yielding cleaned [O III] $\lambda 5008$ flux in those slightly bluer areas within the extraction aperture. This procedure is then conducted iteratively, until the [O III] $\lambda 4960$ fluxes in all spatial pixels within the aperture have been removed, and clean 2D maps of [O III] $\lambda 5008$ and $\text{H}\beta$ can be obtained, *at individual PAs*. Finally, we use ASTRODRIZZLE (Gonzaga 2012) to combine the clean [O III] $\lambda 5008$ and $\text{H}\beta$ maps extracted at multiple PAs. The resultant 2D stamps are drizzled onto a $0''.06$ grid, Nyquist sampling the FWHM of the WFC3 PSF, and astrometrically matched to the corresponding broad-band images. Notably, our custom deblending technique does not rely on any models of the spatial profiles of [O III] emission⁵. This is a critical procedure to account for the orient-specific contaminations of [O III] $\lambda 4960$, which can be over $2\text{-}\sigma$ in some spatial areas within the extraction aperture (see the upper right panel of Fig. 2).

3.3. Stellar mass

We perform SED fitting to the broad-band photometry of our galaxies from the *HST* imaging data obtained by *HFF* or *CLASH*. The FAST software (Kriek et al. 2009) is used to infer stellar mass (M_*), star-formation rate (SFR^S , see Sect. 3.5 for more details), and dust extinction of stellar continuum (A_V^S), based on the Bruzual & Charlot (2003) (BC03) stellar population synthesis models. We assume the Chabrier (2003) initial mass function, constant star formation history, the Calzetti et al. (2000) extinction law, and fixed stellar metallicity being one-fifth solar. Since the majority of our galaxies show strong nebular emission in their rest-frame optical, we need to subtract their *nebular* emission from the corresponding broad-band fluxes to estimate more accurately the level of *stellar* continuum. We convolve the best-fit Gaussian profiles for each EL at the source redshift with the *HST* band-pass throughput, to derive the nebular flux, and then subtract

it from the measured broad-band photometry. In Table 3, we show the observed JH_{140} -band magnitude before this correction and the reduction factor, which is a ratio between the JH_{140} -band flux after and before correcting for nebular emission. We verify that this correction is essential for deriving reliable M_* estimates for galaxies on the low mass end ($M_* < 5 \times 10^9 M_\odot$); without this correction M_* can be overestimated by as much as 0.7 dex. We present the results of our stellar continuum SED fitting in Table 3. Thanks to lensing magnification, our sample extends significantly into the low-mass regime at high z , highly complementary to the targets from ground-based surveys (e.g., *KMOS*^{3D}, Wuyts et al. 2016).

3.4. AGN contamination

In Fig. 3, we rely on the mass-excitation diagram to exclude active galactic nucleus (AGN) candidates from our sample. The demarcation scheme (Juneau et al. 2014) aims to separate AGN from star-forming galaxies, based on the SDSS DR7 emission-line galaxies at $z \sim 0$. This scheme has been shown to reproduce the bivariate distributions seen in a number of high-redshift galaxy samples out to $z \sim 1.5$ (Juneau et al. 2014). We therefore discard sources in our sample that are $2\text{-}\sigma$ away from the star-forming region in the diagram, given the measurement uncertainties on M_* and $[\text{O III}]/\text{H}\beta$. To examine possible redshift-dependent trends in the future Sections, we subdivide our sample into three bins: 39, 24, and 16 galaxies at $z \in [1.2, 1.6]$, $z \in [1.6, 1.9]$, and $z \in [1.9, 2.3]$, respectively, marked by different symbols in Fig. 3.

Moreover, Coil et al. (2015) found that a $+0.75$ dex shift in M_* of the demarcation curves is necessary to match the loci of AGNs and star-forming galaxies in the MOSDEF surveys at $z \sim 2.3$, to account for the redshift evolution of the mass-metallicity relation. On part of the sample, we also obtained $\text{H}\alpha$ gas kinematics from the ground-based Keck OSIRIS observations (Hirtenstein et al. 2018). The integrated measurement of $f_{[\text{N III}]} / f_{\text{H}\alpha}$ is typically ≤ 0.1 at $3\text{-}\sigma$ confidence level, indicative of star-forming regions with no significant AGN contamination. We thus verify that there is no sign of significant AGN ionization in our sample.

3.5. Star-formation rate

We have two methods for estimating star-formation rate (SFR). First of all, SFR can be obtained from the stellar continuum SED fitting outlined in Sect. 3.3. This method is sensitive to the underlying assumptions of star-formation history and stellar population synthesis models adopted in the fitting procedure. Hereafter, we refer to these measurements as SFR^S .

Secondly, SFR can be derived from nebular emission after correcting for dust attenuation. From our Bayesian inference

⁵ We note that in the most up-to-date version of GRIZLI, the subtraction of [O III] $\lambda 4960$ is implemented. However GRIZLI's automatic subtraction is based on a spatial model of [O III] $\lambda 4960$ emission, which is different from our procedure presented here.

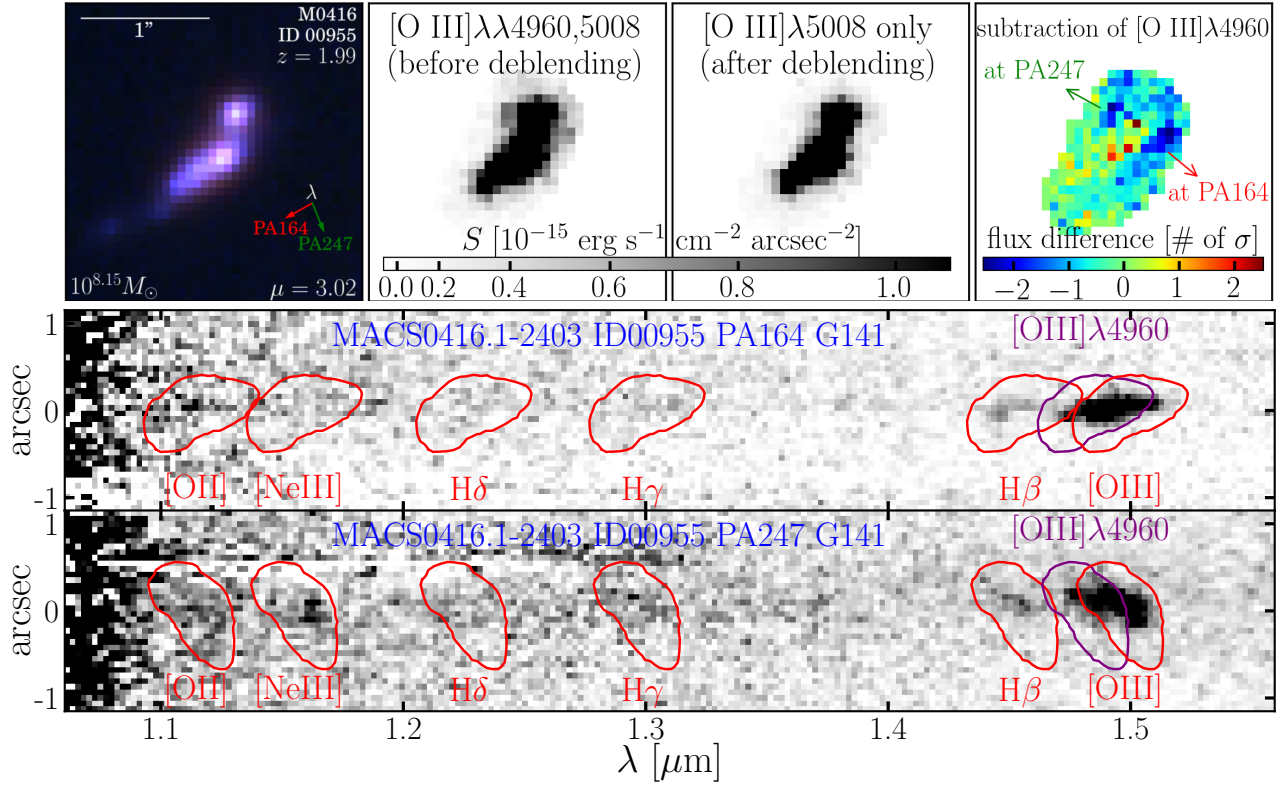


Figure 2. Our custom technique of obtaining pure [O III] $\lambda 5008$ maps combined from multiple orients of grism exposures. **Top**, from left to right: the color-composite image of a $z \sim 2$ dwarf galaxy ($M_* \approx 10^8 M_\odot$), its [O III] map before deblending the [O III] doublets, its pure [O III] $\lambda 5008$ map clean from the partial contamination of [O III] $\lambda 4960$ at two orients (PA164 and PA247), and the significance of difference between these two [O III] maps. The significance is expressed as the flux differences divided by the corresponding flux uncertainties (i.e. σ) of [O III] $\lambda 5008$ in each spatial pixel. **Middle and bottom**: 2D contamination and continuum subtracted G141 spectra of this dwarf galaxy at two orients (PA164 and PA274) separately. Due to the limited spectral resolutions of *HST* grisms and extended source morphology, fluxes of [O III] $\lambda 4960$ are blended into [O III] $\lambda 5008$ and $H\beta$ in a spatially inhomogeneous fashion, specific to the light dispersion direction at individual orients.

method presented in Sect. 3.6, we obtain posterior probability distributions of the de-reddened $H\beta$ flux, which can be converted to the intrinsic $H\alpha$ luminosity given source redshift. As a consequence, SFR (hereafter denoted as SFR^N) can then be calculated following the widely used calibration (Kennicutt 1998), i.e.,

$$\text{SFR}^N = 4.6 \times 10^{-42} \frac{L(H\alpha)}{\text{erg/s}} (M_\odot/\text{yr}), \quad (1)$$

appropriate for the Chabrier (2003) initial mass function. Unlike the measurements from SED fitting, this method provides a proxy of instantaneous star-forming activities on the time scale of ~ 10 Myrs. This short time scale is relevant to probe the highly dynamic feedback processes which are effective in re-distributing metals (see e.g., Hopkins et al. 2014). Therefore, we quote the values of SFR^N as our fiducial SFR measurements if not stated otherwise.

We note that for our low- z sample (39 galaxies at $z \in [1.2, 1.6]$), $H\alpha$ is covered by the WFC3/G141 grism. However, due to the low spectral resolution, it is heavily blended with [N II]. We hence rely on the empirical prescription of

Faisst et al. (2017) to subtract the contribution of [N II] fluxes from the measured $H\alpha$ flux, based on stellar mass and redshift of our galaxies (see Table 3 for the calculated [N II]/ $H\alpha$ flux ratios). This ensures a more reliable estimate of SFR^N , less impacted by dust than the $H\beta$ -based measurements.

On the left panel of Fig. 4, we show the loci of our galaxies in the diagram of SFR vs. M_* . By selecting lensed galaxies via their nebular EL flux, our sample reaches an instantaneous SFR limit of $\sim 1 M_\odot/\text{yr}$ at $z \sim 2$. In comparison to mass-complete samples (from e.g., the *KMOS*^{3D} survey, Wuyts et al. 2016) and galaxies from the star-forming main sequence (SFMS, Speagle et al. 2014; Whitaker et al. 2014), we push the exploration of star-forming galaxies at the cosmic noon by 1-2 dex deeper into the low-mass regime. We also show the loci of the spectral stacks from the WFC3 Infrared Spectroscopic Parallel (WISP) Survey (Henry et al. 2013), very close to that of our galaxies given similar observing strategies. We gain over 1 dex in M_* thanks to lensing magnification and the 14-orbit depth of the *GLASS* data in each field.

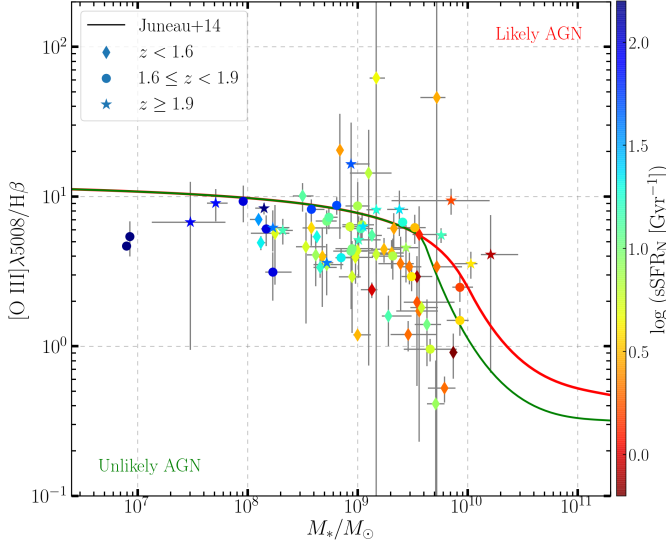


Figure 3. Mass-excitation diagram for our galaxies. The demarcation curves are from Juneau et al. (2014) based on the $z \sim 0$ SDSS DR7 emission-line sample: AGNs are located mainly above the red curve, star-forming galaxies are located below the green curve, and AGN/star-forming composites are in between. Our entire sample is separated into three redshift bins: $z < 1.6$ (39 sources), $1.6 \leq z < 1.9$ (24 sources), and $z \geq 1.9$ (16 sources), color-coded in sSFR. We show that the majority of our sources are located below the green curve, where the possibility of being classified as AGNs is low (<10%).

3.6. Metallicity and its radial gradient

Following our previous work (Wang et al. 2017, 2019), we adopt a Bayesian method to infer simultaneously metallicity ($12 + \log(\text{O}/\text{H})$), nebular dust extinction (A_V^N) and de-reddened $\text{H}\beta$ flux ($f_{\text{H}\beta}$), based on observed EL fluxes directly, as measured in Sect. 3.1. This approach is superior to converting EL flux ratios (e.g., R_{23} , O_{32}) to metallicity, because it properly takes into account any weak nebular emission that falls short of the detection limit, and avoids double counting information as it happens when combining multiple flux ratios that involve the same line. The MCMC sampler EMCEE is used to explore the parameter space, with the likelihood function defined as

$$L \propto \exp(-\chi^2/2) = \exp\left(-\frac{1}{2} \cdot \sum_i \frac{(f_{\text{EL}_i} - R_i \cdot f_{\text{H}\beta})^2}{(\sigma_{\text{EL}_i})^2 + (f_{\text{H}\beta})^2 \cdot (\sigma_{R_i})^2}\right). \quad (2)$$

Here EL_i represents each of the available ELs, among the set of $[\text{O II}]$, $\text{H}\gamma$, $\text{H}\beta$, $[\text{O III}]$, $\text{H}\alpha$, $[\text{S II}]$. f_{EL_i} and σ_{EL_i} denote the EL_i flux and its uncertainty, de-reddened given a value of A_V^N drawn from the MCMC sampling. The Cardelli et al. (1989) galactic extinction law with $R_V = 3.1$ is adopted to correct for dust reddening. R_i is the expected flux ratio between EL_i and $\text{H}\beta$, with σ_{R_i} being its intrinsic scatter. The con-

tent of R_i varies from strong-line diagnostic to Balmer decrement depending on the associated EL_i . In practice, if EL_i is one of the Balmer lines, R_i is given by $\text{H}\alpha/\text{H}\beta = 2.86$ and $\text{H}\gamma/\text{H}\beta = 0.47$, i.e., the Balmer decrement ratios assuming case B recombination under fiducial H II region situations. Instead, if EL_i is one of the oxygen collisionally excited lines, we take the strong-line flux ratios (i.e. $f_{[\text{O III}]} / f_{\text{H}\beta}$ and $f_{[\text{O II}]} / f_{\text{H}\beta}$) calibrated by Maiolino et al. (2008) as R_i . Last, if EL_i is $[\text{S II}]$, we rely on our strong-line calibration of $[\text{S II}]/\text{H}\alpha$ presented in Wang et al. (2017).

This Bayesian inference is first performed on the integrated EL fluxes measured for each galaxy, to yield global metallicity. On the right panel of Fig. 4, we show the mass-metallicity relation (MZR) from our sample, color-coded by the specific SFR ($\text{sSFR} = \text{SFR}/M_*$) obtained from the aforementioned analyses. We also overlay the MZR from the WISP survey derived using the same strong-line calibrations (Henry et al. 2013). It is encouraging to see that the two MZR follow similar trends, due to similar source selection technique and observing strategy. Notably, our galaxies at the extreme low-mass end ($M_* \lesssim 10^9 M_\odot$) show both elevated metallicity and sSFR. This is consistent with the hypothesis that these low-mass systems are in the phase of early mass assembly with efficient metal enrichment and minimum dilution from pristine gas infall.

In addition to the integrated EL fluxes, from the procedures described in Sect. 3.2, we also obtain 2D spatial distributions of EL surface brightnesses. We utilize Voronoi tessellation as in Wang et al. (2019) to divide spatial bins with nearly uniform SNRs of the strongest EL available (usually $[\text{O III}]$). Our spatially resolved analysis based on Voronoi tessellation is superior to averaging the signals in radial annuli, because of azimuthal variations (as large as 0.2 dex) in metallicity spatial distribution in nearby spiral galaxies (Berg et al. 2015; Ho et al. 2017). Our Bayesian inference is then executed in each of the Voronoi bins for all sources, yielding their metallicity maps at sub-kpc resolution.

To get the intrinsic deprojected galactocentric distance scale for each Voronoi bin, we conduct detailed reconstructions of the source-plane morphology of each galaxy in our sample. We first obtain a 2D map of stellar surface density (Σ_* , e.g., as shown in Fig. 5) for each source through pixel-by-pixel SED fitting following the prescription described in Sect. 3.3. Then the pixels in this map are ray-traced back to their source plane positions, according to the deflection fields given by the macroscopic cluster lens models. For all the *HFF* clusters, we use the SHARON & JOHNSON version 4corr models (Johnson et al. 2014). For the *CLASH*-only clusters except RXJ1347, we use the Zitrin PIEMD+eNFW version 2 model. For RXJ1347, we use our own model built following closely the approach in Johnson et al. (2014). To this de-lensed 2D Σ_* map, we fit an elliptical Gaussian function, to

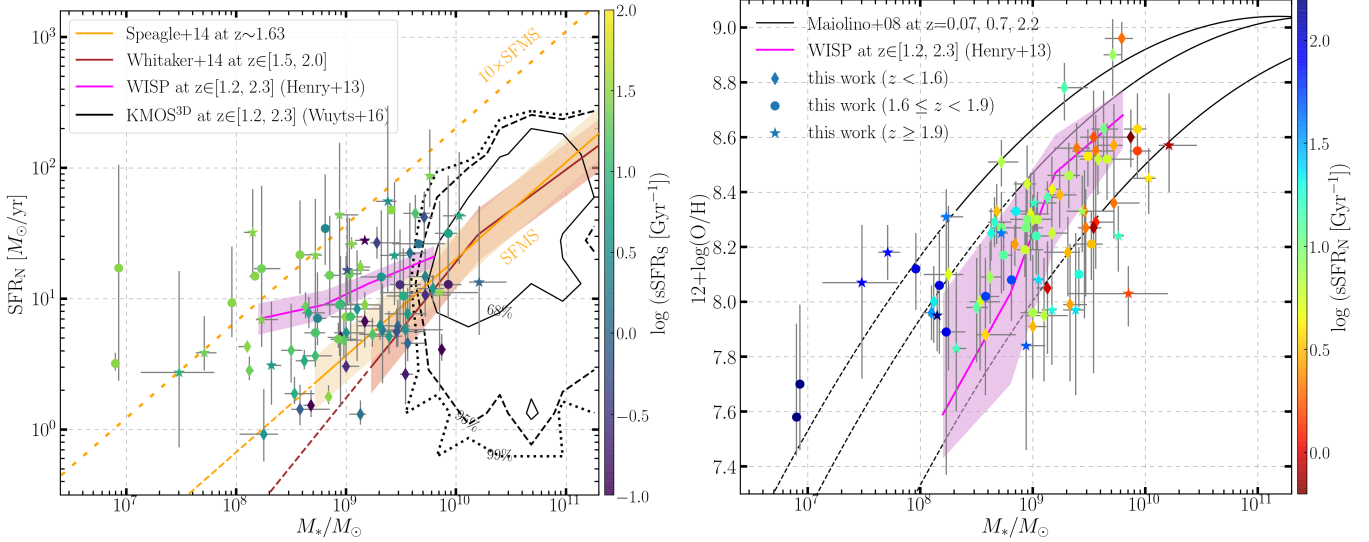


Figure 4. Global properties of our sample. **Left:** SFR as a function of M_* for galaxies at cosmic noon. Our galaxies are represented by the symbols following the scheme in Fig. 3 corresponding to different z bins. However the color coding reflects the specific SFR derived from stellar continuum SED fitting, after subtracting EL fluxes (see Sect. 3.3). The loci of our galaxies are consistent with that of the WISP survey (Henry et al. 2013), if the SFR inferred from dust-corrected nebular emission is adopted. We also show that in terms of mass coverage, our sample is highly complementary to the ground-based mass-complete sample of KMOS^{3D}, which can only probe down to $\sim 5 \times 10^9 M_\odot$ at $z \sim 2$. **Right:** mass-metallicity relations for high- z galaxies. The symbols of our sample now have the same color-coding as in Fig. 3. Our galaxies follow similar trends of the MZR from the WISP survey and Maiolino et al. (2008). In the low mass regime ($M_* \lesssim 10^8 M_\odot$), our galaxies are more metal enriched than the simple extensions of those MZR. These metal-enriched galaxies also have higher sSFR than the sample average.

determine inclination, axis ratio, and major axis orientation, so that the source intrinsic morphology is recovered from lensing distortion. Since we have measured both metallicity and source-plane de-projected galactocentric radius for each Voronoi bin, we can estimate a radial gradient slope via linear regression. Fig. 5 demonstrates the entire process for measuring the metallicity radial gradient of a $z \sim 2$ star-forming dwarf galaxy.

In the end, we secure a total of 79 galaxies in the redshift range of $1.2 \lesssim z \lesssim 2.3$ with sub-kpc resolution metallicity gradients (see Table 1 for the numbers of sources in individual cluster center fields). This is hitherto the largest sample of such measurements in the distant Universe. This sample enables robust measures of both average gradient slopes and scatter in the population.

4. THE COSMIC EVOLUTION OF METALLICITY GRADIENTS AT HIGH REDSHIFTS

In this section, we collect published results on radial gradients of metallicity measured in the distant Universe. We focus on the measurements that are derived with sub-kpc resolution, because insufficient spatial sampling is shown to cause spuriously flat gradient measurements (Yuan et al. 2013). This poses a real challenge for ground-based observations, given the optimal seeing condition is $\sim 0''.6$, equivalent to 5 kpc at $z \sim 2$. There have been a number of attempts to overcome this beam smearing through correcting the dis-

torted light wave front with the adaptive optics (AO) technique. Using the *SINFONI* instrument on the *VLT* under the AO mode, Swinbank et al. (2012) measured 7 gradients at $z \sim 1.5$. Following the same strategy, Förster Schreiber et al. (2018) expanded the sample by adding 21 new measurements at $z \sim 2$ from the SINS/zC-SINF survey⁶. Lensing can also help increase the spatial sampling rate. Jones et al. (2013) pioneered this approach by securing 4 gradients at $z \sim 2$ in galaxy-galaxy lensing systems using the AO-assisted *OSIRIS* instrument on the *Keck* telescope, with resolution further boosted $\gtrsim 3\times$ by lensing magnification. Leethochawalit et al. (2016) carried out similar analyses and measured 11 new gradients at similar redshifts. To recap, there exist a total of 43 metallicity gradient measurements with sub-kpc spatial resolution at cosmic noon before our work.

In this work, we *triple* the sample size by presenting 79 sub-kpc resolution metallicity radial gradients in star-forming galaxies at cosmic noon. This is by far the largest homogeneous sample with sufficient spatial resolution, which enables a uniform analysis. In Fig. 6, our results are highlighted by three sets of symbols — corresponding to the three z sub-groups — color-coded in sSFR. At 2- σ con-

⁶ Note that Förster Schreiber et al. (2018) only published the radial gradients of $[\text{N II}]/\text{H}\alpha$ measured in their sample galaxies. We convert those measurements into metallicity gradients following the widely adopted strong line calibration of Pettini & Pagel (2004).

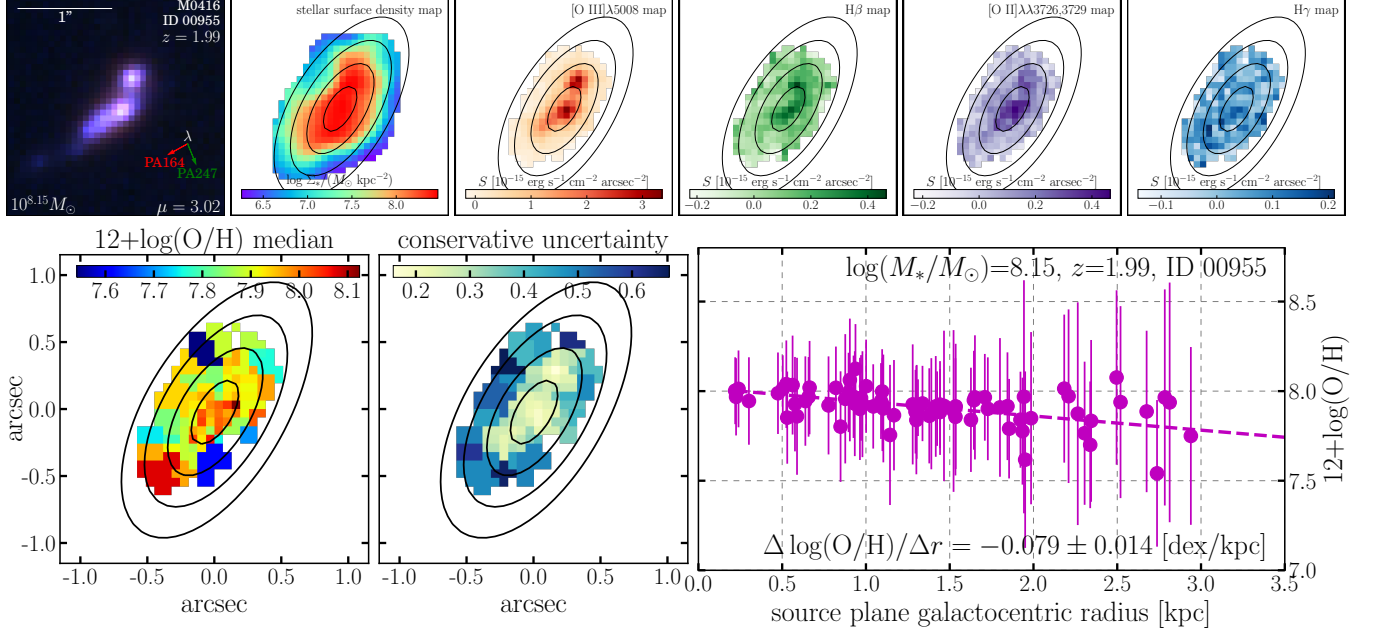


Figure 5. A $z \sim 2$ star-forming dwarf galaxy ($M_* \approx 10^8 M_\odot$) with a negative metallicity radial gradient, similar to that measured in our Milky Way (i.e., -0.07 ± 0.01 , Smartt & Rolleston 1997). We show this as an example of the analysis procedures applied to our entire sample. **Top**, from left to right: color composite stamp (from the *HFF* imaging), stellar surface density (Σ_*) map (obtained from pixel-by-pixel SED fitting to *HFF* photometry), and surface brightness maps of ELs [O III], $H\beta$, [O II], and $H\gamma$. We use the technique demonstrated in Fig. 2 to obtain pure [O III] $\lambda 5008$ and $H\beta$ maps for the source. The black contours mark the de-lensed de-projected galacto-centric radii with 1 kpc interval, given by our source plane morphological reconstruction described in Sect. 3.6. **Bottom**: metallicity map and radial gradient determination for this galaxy. The weighted Voronoi tessellation technique (Cappellari & Copin 2003; Diehl & Statler 2006) is adopted to divide the surface into spatial bins with a constant SNR of 5 on [O III]. In the right panel, the metallicity measurements in these Voronoi bins are plotted as magenta points. The dashed magenta line denotes the linear regression, with the corresponding slope shown at the bottom. The spatial extent and orientation remain unchanged throughout all the 2D maps in both rows, with north up and east to the left.

fidence level, our measurements show 14/79 (18%) negative, 7/79 (9%) inverted, and 58/79 (73%) flat gradients, respectively. All individual ground-based measurements at similar resolution ($\lesssim \text{kpc}$ scale) are represented by magenta squares.

Some theoretical trends are overlaid in Fig. 6. In particular, two numerical simulations with different galactic feedback strengths but otherwise identical settings by Gibson et al. (2013) are shown as the orange curves. The comparison between these two trends demonstrates that enhanced feedback can be highly efficient in erasing metal inhomogeneity. Therefore resolved chemical properties, if measured accurately, can shed light on the strength of galactic feedback in the early phase of disk growth.

Fig. 6 also shows the spread of the *KMOS*^{3D} gradient measurements by Wuyts et al. (2016), which is highly clustered to flatness. However, without AO support nor lensing magnification, gradient measurements in typical field galaxies under natural seeing provide limited information for physical interpretation. To mitigate the potential bias from beam smearing, Carton et al. (2018) conducted a forward-modeling analysis to recover 65 gradients at $0.1 \lesssim z \lesssim 0.8$ from the seeing-limited *MUSE* observations (marked in green in Fig. 6).

The $2\text{-}\sigma$ interval of the FIRE simulations (Ma et al. 2017) is shown as the grey-shaded region in Fig. 6. We see that the scatter predicted by the FIRE simulations matches well that from low- z observations (at $z \lesssim 1$, e.g., from Carton et al. 2018), but it is smaller by a factor of 2 at higher redshifts, especially at $z \gtrsim 1.3$. This likely reflects that galaxies display more diverse chemo-structural properties at the peak epoch of cosmic structure formation and metal enrichment, when star formation is more episodic and vigorous (see e.g., Hopkins et al. 2014).

5. THE MASS DEPENDENCE OF METALLICITY GRADIENTS AT SUB-KPC RESOLUTION: TESTING THEORIES OVER 4 DEX OF M_*

With the sample statistics greatly improved, we can quantify the mass dependence of reliably measured metallicity gradients at high redshifts, as a test of theoretical predictions. The combined sample includes our 79 measurements at $z \in [1.2, 2.3]$, and 35⁷ others' as given in Sect. 4. Following the same color/marker styles as in Fig. 6, we plot these

⁷ Only 3/11 gradients reported in Leethochawalit et al. (2016) have M_* measured.

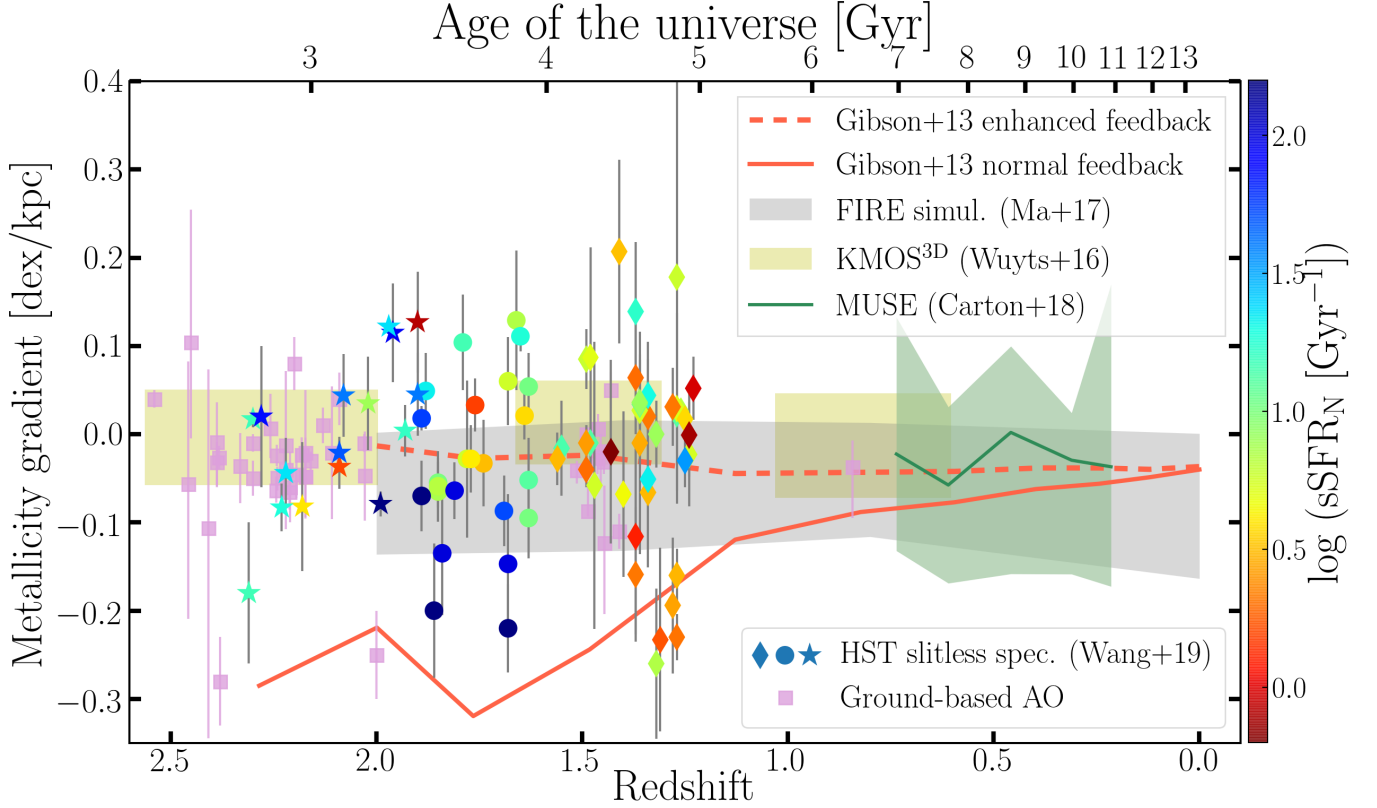


Figure 6. Overview of metallicity gradients in the distant Universe. Our measurements are represented by three symbols, corresponding to different z ranges as in Fig. 3, color-coded in sSFR. As a comparison, we also include individual measurements at similar resolution ($\lesssim \text{kpc}$ scale) from ground-based AO-assisted observations, marked by magenta squares (Swinbank et al. 2012; Jones et al. 2013; Leethochawalit et al. 2016; Förster Schreiber et al. 2018). The $2\text{-}\sigma$ spreads of measurements from $\text{KMOS}^{3\text{D}}$ (Wuyts et al. 2016) and MUSE (Carton et al. 2018), and the simulation results from FIRE (Ma et al. 2017), are shown as shaded regions in green, yellow, and grey, respectively. The evolutionary tracks of two simulated disk galaxies (Milky Way analogs at $z \sim 0$) with different feedback strength but otherwise identical numerical setup are denoted by the two orange curves.

high-resolution gradient measurements as a function of their associated M_* in Fig. 7. It is remarkable that now the observational data cover *four orders of magnitude* in M_* . Notably, over half of our gradient measurements reside in the dwarf mass regime ($M_* \lesssim 2 \times 10^9 M_\odot$), probing $\gtrsim 2$ dex deeper into the low-mass end, compared with the ground-based AO results (magenta squares).

We perform linear regression on all these measurements of metallicity gradient and stellar mass, with errors on both quantities taken into account, using the following formula,

$$\Delta \log(\text{O}/\text{H})/\Delta r [\text{dex kpc}^{-1}] = \alpha + \beta \log(M_*/M_{\text{med}}) + N(0, \sigma^2). \quad (3)$$

Here α and β are the intercept and the slope of the linear function, respectively. $N(0, \sigma^2)$ represents a normal distribution with σ being the intrinsic scatter in units of dex kpc^{-1} . M_{med} is the median of the input stellar masses taken as normalization. For the entire mass range (where $M_{\text{med}} = 10^{9.4} M_\odot$), we obtain the following estimates: $\alpha = -0.020 \pm 0.007$, $\beta = -0.014 \pm 0.008$, $\sigma = 0.060 \pm 0.006$ (see the result of

Case I in Table 2). This shows a weak negative correction between metallicity gradient and stellar mass for these 114 high- z star-forming galaxies.

To understand this negative mass dependence, we show two theoretical predictions from the EAGLE simulations in Fig. 7, corresponding to two suites of numerical simulations implementing different strengths of supernova feedback (Tissera et al. 2018). We see a drastic difference in the slope of the mass dependence of metallicity gradients predicted by different feedback settings in EAGLE, albeit the short M_* coverage. This difference is largely caused by the bifurcations seen in the temporal evolutions of radial chemical profiles for individual galaxies, exemplified by the two simulation tracks shown in Fig. 6. Under the assumption of weak feedback, galaxies evolve according to secular processes, and their radial gradients flatten over time (Pilkington et al. 2012). Given mass assembly down-sizing, more massive galaxies are in a later phase of disk growth than less massive ones (Brinchmann et al. 2004). Collectively, a positive mass dependence of radial gradients manifests. How-

ever, when feedback is enhanced, feedback-driven gas flows can efficiently mix stellar nucleosynthesis yields and prevent any metal inhomogeneity from emerging (Ma et al. 2017). This effect is more pronounced in lower mass galaxies living in smaller dark matter halos with shallower gravitational potentials. As a result, a generally negative mass dependence (flat/inverted gradients at low-mass end and negative gradients at high-mass end) can be anticipated.

Fig. 7 also shows the $2\text{-}\sigma$ spread of the mass dependence from the FIRE simulations (Ma et al. 2017). Given the relatively strong feedback scheme implemented in FIRE, we expect a negative mass dependence, which is indeed seen. Remarkably, the predictions of the FIRE simulations match very well the linear regression fit based on the combined high- z metallicity gradient sample, strongly supporting that enhanced feedback — not secular processes — plays a significant role in shaping the chemical enrichment and structural evolution during the disk mass assembly (Hopkins et al. 2014; Vogelsberger et al. 2014).

To verify that the observed trends are robust, we subdivide the gradient measurements into three mass bins and perform a separate linear regression analysis to each bin. The results are given in Table 2. We see that the intercept value becomes more negative as M_* increases, with the slopes all consistent with zero, confirming the negative mass dependence of metallicity gradients over the entire mass range. More importantly, we observe an increase in the intrinsic scatter of metallicity gradients with M_* from high-mass to low-mass regimes, consistent with the findings in local spiral galaxies by Bresolin (2019). This increase in scatter can also be found if separating the galaxies based on their sSFR⁸. For galaxies in the combined sample with $\text{sSFR} \gtrsim 5 \text{ Gyr}^{-1}$, the scatter is constrained to be $\sigma = 0.082^{+0.013}_{-0.011}$ (case IVa in Table 2) whereas for galaxies with $\text{sSFR} \lesssim 5 \text{ Gyr}^{-1}$, the scatter is instead $\sigma = 0.048^{+0.007}_{-0.006}$ (case IVb in Table 2).

The increase of sSFR in low-mass systems can be ascribed to the accretion of low-metallicity gas from the cosmic filaments (i.e., cold-mode gas accretion, Dekel et al. 2009), or gravitational interaction events amplifying the star-formation efficiency (i.e., merger-induced starbursts, Stott et al. 2013). Both of them can bring about large dispersions in the radial chemical profiles. To investigate which one of the two effects is more dominant in boosting the chemo-structural diversity in low-mass high-sSFR galaxies, we turn to the global MZR of our sample, presented in Section 3.6 (see Fig. 4). We rely on the WISP measurements as the control sample, because of the similar source selection criteria, mass coverage, redshift range, and consistent techniques in estimating SFR (based on

Balmer line fluxes) and metallicity (assuming the Maiolino et al. (2008) calibrations).

We find that in the medium-mass bin ($M_*/M_\odot \in [10^9, 10^{10}]$), the galaxies in our sample with higher SFR than that of the WISP stacks, are more metal-poor by 0.15 dex than the WISP metallicities in the corresponding mass range. This is supportive of the cold-mode accretion diluting the global metallicity of our galaxies, stimulating star formation and increasing the intrinsic scatter of metallicity gradients. However, in the low-mass bin ($M_*/M_\odot \in [10^8, 10^9]$), our galaxies with higher SFR than WISP show significant metal-enrichment, i.e., higher by 0.27 dex than the corresponding WISP metallicities. We hence argue that in the dwarf-mass regime of $M_* \lesssim 10^9 M_\odot$, merger-driven starbursts play a more predominant role than the cold-mode accretion does to boost the chemo-structural diversity. Our result is consistent with the sharp increase of the merger fraction — from 10% to over 50% for galaxies at $M_* \sim 10^{10}$ to $10^{8.5}$ at $z \sim 1.5$ — found by the HiZELS survey (Stott et al. 2013, 2014). For part of our dwarf galaxies on which we have mapped their gas kinematics using Keck OSIRIS, we also found that the velocity field becomes more turbulent (i.e. with lower ratios of rotational speed versus velocity dispersion) for galaxies with higher sSFR (Hirtenstein et al. 2018). This kinematic evidence further reinforces the scenario that mergers boost the star-formation efficiency, random motions, and the chemo-structural diversity in dwarf galaxies at cosmic noon.

Lastly, the combined high- z metallicity gradient sample reveals that inverted gradients are almost exclusively found in the low-mass range, i.e., $M_* \lesssim 3 \times 10^9$ (also see Carton et al. 2018). This feature is also seen in the local Universe: only the lowest M_* bin (at $\sim 10^9 M_\odot$) from the MaNGA survey shows positive gradient slope (Belfiore et al. 2017). The reason for inverted gradients in isolated systems is still under debate, with possible causes ranging from centrally-directed cold-mode accretion (Cresci et al. 2010), or metal-loaded outflows triggered by galactic winds (Wang et al. 2019). In any case, these processes should be more pronounced in low-mass systems, suggested by the occurrence rate of this inverted gradient phenomenon.

6. CONCLUSION

To summarize, we have presented an unprecedentedly large sample of sub-kpc resolution metallicity radial gradients in 79 gravitationally-lensed star-forming galaxies at $1.2 \lesssim z \lesssim 2.3$, using *HST* NIR slitless spectroscopy. We performed state-of-the-art reduction of grism data, careful stellar continuum SED fitting after subtracting nebular emission from broad-band photometry, and Bayesian inferences of metallicity and SFR based on EL fluxes. Our sample spans a M_* range of $[10^7, 10^{10}] M_\odot$, an instantaneous SFR range of $[1, 100] M_\odot/\text{yr}$, and a global metallicity range

⁸ Here we use the SED-derived SFR, i.e., SFR^{SED} in Table 3, for our galaxies to be self-consistent throughout the combined sample.

Table 2. Linear regression results of the mass dependence of metallicity radial gradients at cosmic noon

Case	α	β	σ	$M_{\text{med}}[M_{\odot}]$	N_{source}	Notes
I	$-0.0198^{+0.0069}_{-0.0070}$	$-0.0142^{+0.0079}_{-0.0079}$	$0.0601^{+0.0063}_{-0.0057}$	$10^{9.4}$	114	all metallicity gradients measured at sub-kpc resolution
II	$-0.0125^{+0.0092}_{-0.0095}$	$0.0004^{+0.0188}_{-0.0187}$	$0.0665^{+0.0085}_{-0.0078}$	$10^{9.0}$	79	all metallicity gradients from <i>HST</i> spectroscopy
IIIa	$-0.0403^{+0.0082}_{-0.0085}$	$-0.0052^{+0.0188}_{-0.0182}$	$0.0354^{+0.0084}_{-0.0063}$	$10^{10.4}$	28	high-mass bin: $M_*/M_{\odot} \gtrsim 10^{10}$
IIIb	$-0.0088^{+0.0132}_{-0.0132}$	$-0.0545^{+0.0557}_{-0.0553}$	$0.0768^{+0.0117}_{-0.0101}$	$10^{9.5}$	48	medium-mass bin: $10^9 \lesssim M_*/M_{\odot} \lesssim 10^{10}$
IIIc	$-0.0198^{+0.0142}_{-0.0139}$	$0.0224^{+0.0491}_{-0.0495}$	$0.0597^{+0.0148}_{-0.0128}$	$10^{8.6}$	32	low-mass bin: $10^8 \lesssim M_*/M_{\odot} \lesssim 10^9$
IVa	$-0.0133^{+0.0130}_{-0.0129}$	$0.0204^{+0.0168}_{-0.0165}$	$0.0825^{+0.0126}_{-0.0111}$	$10^{8.9}$	50	high-sSFR bin: $\text{sSFR} \gtrsim 5\text{Gyr}^{-1}$
IVb	$-0.0321^{+0.0078}_{-0.0083}$	$-0.0073^{+0.0095}_{-0.0094}$	$0.0478^{+0.0074}_{-0.0064}$	$10^{9.7}$	64	low-sSFR bin: $\text{sSFR} \lesssim 5\text{Gyr}^{-1}$

NOTE—The linear regression is performed using the LINMIX software^a taking into account the measurement uncertainties on both stellar mass (M_*) and metallicity gradient ($\Delta \log(\text{O}/\text{H})/\Delta r$), following the Bayesian method proposed by Kelly (2007). The following function form (Eq. 3) is adopted: $\Delta \log(\text{O}/\text{H})/\Delta r [\text{dex kpc}^{-1}] = \alpha + \beta \log(M_*/M_{\text{med}}) + \text{N}(0, \sigma^2)$. As given in the rightmost column, Cases I corresponds to the linear regression result based on all sub-kpc scale metallicity gradient measurements at the cosmic noon epoch, whereas Case II shows the result from our gradient measurements only. We divide the entire sample into three M_* bins and conduct linear regressions separately, with results represented by Cases IIIa,b,c. Cases IVa,b show the results if the entire sample is divided based on sSFR, instead of M_* . The number of sources (N_{source}) involved in each case is shown in the second rightmost column.

^a <https://github.com/jmeyers314/linmix>

of $7.6 \lesssim 12 + \log(\text{O}/\text{H}) \lesssim 9.0$, i.e., $[\frac{1}{12}, 2]$ solar. At 2- σ confidence level, we secured 14 and 7 galaxies that show negative and inverted gradients, respectively. Collecting all high resolution gradient measurements at high redshifts currently existing (where results presented in this work constitute 2/3 of all measurements), we measure a weak negative mass dependence over four orders of magnitude in M_* : $\Delta \log(\text{O}/\text{H})/\Delta r [\text{dex kpc}^{-1}] = (-0.020 \pm 0.007) + (-0.014 \pm 0.008) \log(M_*/10^{9.4} M_{\odot})$ with $\sigma = 0.060 \pm 0.006$ being the intrinsic scatter. This supports enhanced feedback as the main driver of the chemo-structural evolution of star-forming galaxies at cosmic noon. Moreover, we also find that the intrinsic scatter of metallicity gradients increases with decreasing M_* and increasing sSFR. Combined with the global metallicity measurements, our result is consistent with the hypothesis that the combined effect of cold-mode gas accretion and merger-induced starbursts strongly boosts the chemo-structural diversity of low-mass star-forming galaxies at cosmic noon, with mergers playing a much more predominant role in the dwarf-mass regime of $M_* \lesssim 10^9 M_{\odot}$. This work demonstrates that by accurately mapping the radial chemical profiles of star-forming galaxies at high redshifts, we can cast strong constraints on the role that feedback, gas flows and mergers play in the early phase of disk

mass assembly. The observed trends between metallicity and galaxy properties, while weak, are nonetheless very well measured over a wide dynamic range of mass. This census offers a stringent test for theoretical models and cosmological simulations, as the resulting trends are highly sensitive to baryon cycling processes at the peak of cosmic star formation ($1.2 \lesssim z \lesssim 2.3$). Using the Near-Infrared Imager and Slitless Spectrograph (NIRISS) onboard the soon-to-be-launched James Webb Space Telescope (*JWST*), the GLASS-*JWST* ERS program (PI Treu, ID 1324) and the Canadian NIRISS Unbiased Cluster Survey (CANUCS) GTO program (PI Willott) will conduct *K*-band slitless spectroscopy on several galaxy cluster center fields. The data acquired by these programs will enable sub-kpc resolution measurements of metallicity gradients to $z \lesssim 3.5$, and thus extend the test for theoretical predictions to even higher redshifts.

ACKNOWLEDGMENTS

This work is supported by NASA through HST grant HST-GO-13459. XW acknowledges support by UCLA through a dissertation year fellowship.

REFERENCES

- Belfiore, F., Maiolino, R., Tremonti, C. A., et al. 2017, Monthly Notices of the Royal Astronomical Society, 469, 151
- Berg, D. A., Skillman, E. D., Croxall, K. V., et al. 2015, The Astrophysical Journal, 806, 16
- Bresolin, F. 2019, eprint arXiv:1907.05071, 1907.05071
- Brinchmann, J., Charlot, S., White, S. D. M., et al. 2004, Monthly Notices of the Royal Astronomical Society, 351, 1151
- Bruzual, G., & Charlot, S. 2003, Monthly Notices of the Royal Astronomical Society, 344, 1000

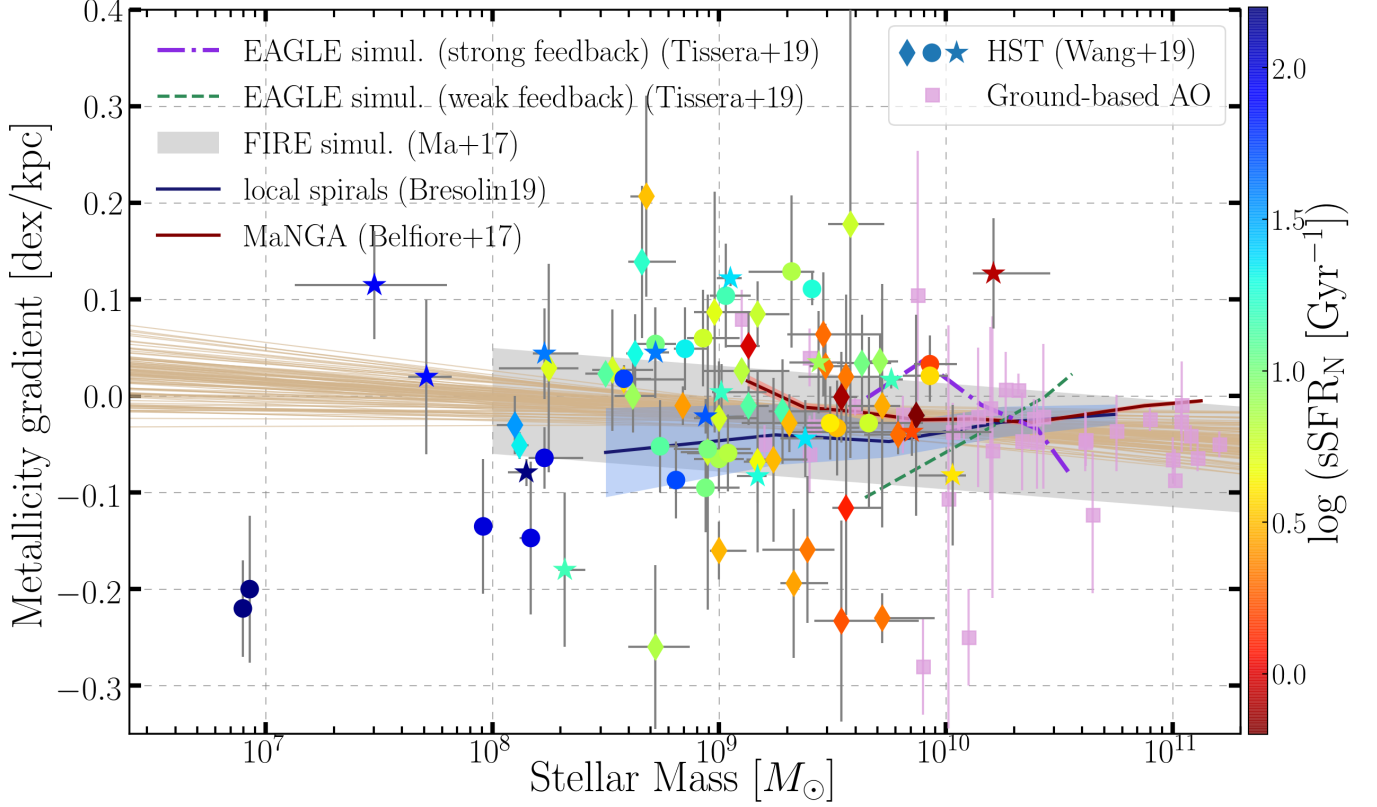


Figure 7. Metallicity gradient as a function of stellar mass for high- z and local star-forming galaxies. As in Fig. 6, our measurements are represented by three types of symbols regarding three z bins colored coded in sSFR, whereas high- z ground-based measurements with similar resolution are denoted by magenta squares. For comparison, we also show the median measurements with $1\text{-}\sigma$ interval of local measurements (Belfiore et al. 2017; Bresolin 2019), the $2\text{-}\sigma$ spread of the FIRE simulations (Ma et al. 2017), and two mass dependencies derived from the EAGLE simulations assuming different feedback settings (Tissera et al. 2018). Combining all available high- z gradients measured at sufficient spatial resolution ($\lesssim \text{kpc}$), we obtain a weakly negative mass dependence over four orders of magnitude in M_* : $\Delta \log(\text{O}/\text{H})/\Delta r [\text{dex kpc}^{-1}] = (-0.020 \pm 0.007) + (-0.014 \pm 0.008) \log(M_*/10^{9.4} M_\odot)$ with the intrinsic scatter being $\sigma = 0.060 \pm 0.006$. The thin lines in tan mark 100 random draws from the linear regression. This observed mass dependence is in remarkable agreement with the predictions of the FIRE simulations. However, as shown in Table 2, we also observe an increase of the intrinsic scatter from high-mass to low-mass systems, not captured by theoretical predictions.

Calzetti, D., Armus, L., Bohlin, R. C., et al. 2000, *The Astrophysical Journal*, 533, 682

Cappellari, M., & Copin, Y. 2003, *Monthly Notices of the Royal Astronomical Society*, 342, 345

Cardelli, J. A., Clayton, G. C., & Mathis, J. S. 1989, *The Astrophysical Journal*, 345, 245

Carton, D., Brinchmann, J., Contini, T., et al. 2018, *Monthly Notices of the Royal Astronomical Society*, 1805.08131

Chabrier, G. 2003, *Publications of the Astronomical Society of the Pacific*, 115, 763

Coil, A. L., Aird, J., Reddy, N. A., et al. 2015, *The Astrophysical Journal*, 801, 35

Cresci, G., Mannucci, F., Maiolino, R., et al. 2010, *Nature*, 467, 811

Davé, R., Finlator, K., & Oppenheimer, B. D. 2012, *Monthly Notices of the Royal Astronomical Society*, 421, 98

Dekel, A., & Mandelker, N. 2014, *Monthly Notices of the Royal Astronomical Society*, 444, 2071

Dekel, A., Birnboim, Y., Engel, G., et al. 2009, *Nature*, 457, 451

Diehl, S., & Statler, T. S. 2006, *Monthly Notices of the Royal Astronomical Society*, 368, 497

Erb, D. K. 2015, *Nature*, 523, 169

Faisst, A. L., Masters, D. C., Wang, Y., et al. 2017, eprint arXiv:1710.00834, 1710.00834

Finlator, K., & Davé, R. 2008, *Monthly Notices of the Royal Astronomical Society*, 385, 2181

Förster Schreiber, N. M., Renzini, A., Mancini, C., et al. 2018, eprint arXiv:1802.07276, 1802.07276

Gibson, B. K., Pilkington, K., Brook, C. B., Stinson, G. S., & Bailin, J. 2013, *Astronomy and Astrophysics*, 554, A47

Gonzaga, S. 2012, *The DrizzlePac Handbook*, HST Data Handbook

- Henry, A. L., Scarlata, C., Domínguez, A., et al. 2013, *The Astrophysical Journal*, 776, L27
- Hirtenstein, J., Jones, T. A., Wang, X., et al. 2018, eprint arXiv:1811.11768, 1811.11768
- Ho, I. T., Seibert, M., Meidt, S. E., et al. 2017, *The Astrophysical Journal*, 846, 39
- Hopkins, P. F., Kereš, D., Onorbe, J., et al. 2014, *Monthly Notices of the Royal Astronomical Society*, 445, 581
- Johnson, T. L., Sharon, K., Bayliss, M. B., et al. 2014, *The Astrophysical Journal*, 797, 48
- Jones, T. A., Ellis, R. S., Richard, J., & Jullo, E. 2013, *The Astrophysical Journal*, 765, 48
- Jones, T. A., Wang, X., Schmidt, K. B., et al. 2015, *The Astronomical Journal*, 149, 107
- Juneau, S., Bournaud, F., Charlot, S., et al. 2014, *The Astrophysical Journal*, 788, 88
- Kelly, B. C. 2007, *The Astrophysical Journal*, 665, 1489
- Kennicutt, R. C. J. 1998, *Annual Review of Astronomy and Astrophysics*, 36, 189
- Kriek, M. T., van Dokkum, P. G., Franx, M., Illingworth, G. D., & Magee, D. K. 2009, *The Astrophysical Journal*, 705, L71
- Leethochawalit, N., Jones, T. A., Ellis, R. S., et al. 2016, *The Astrophysical Journal*, 820, 84
- Lilly, S. J., Carollo, C. M., Pipino, A., Renzini, A., & Peng, Y.-j. 2013, *The Astrophysical Journal*, 772, 119
- Lotz, J. M., Koekemoer, A. M., Coe, D., et al. 2016, 1605.06567
- Ma, X., Hopkins, P. F., Feldmann, R., et al. 2017, *Monthly Notices of the Royal Astronomical Society*, 466, 4780
- Madau, P., & Dickinson, M. E. 2014, *Annual Review of Astronomy and Astrophysics*, 52, 415
- Maiolino, R., & Mannucci, F. 2018, 1811.09642
- Maiolino, R., Nagao, T., Grazian, A., et al. 2008, *Astronomy and Astrophysics*, 488, 463
- Peng, Y.-j., & Maiolino, R. 2014, *Monthly Notices of the Royal Astronomical Society*, 443, 3643
- Pettini, M., & Pagel, B. E. J. 2004, *Monthly Notices of the Royal Astronomical Society*, 348, L59
- Pilkington, K., Few, C. G., Gibson, B. K., et al. 2012, *Astronomy and Astrophysics*, 540, A56
- Poetrodjojo, H. M., Groves, B. A., Kewley, L. J., et al. 2018, *Monthly Notices of the Royal Astronomical Society*
- Postman, M., Coe, D., Benítez, N., et al. 2012, *The Astrophysical Journal Supplement Series*, 199, 25
- Sanchez, S. F., Rosales-Ortega, F., Iglesias-Páramo, J., et al. 2014, *Astronomy and Astrophysics*, 563, A49
- Schmidt, K. B., Treu, T. L., Brammer, G. B., et al. 2014, *The Astrophysical Journal Letters*, 782, L36
- Smartt, S. J., & Rolleston, W. R. J. 1997, *The Astrophysical Journal*, 481, L47
- Speagle, J. S., Steinhardt, C. L., Capak, P. L., & Silverman, J. D. 2014, *The Astrophysical Journal Supplement Series*, 214, 15
- Storey, P. J., & Zeppen, C. J. 2000, *Monthly Notices of the Royal Astronomical Society*, 312, 813
- Stott, J. P., Sobral, D., Smail, I. R., et al. 2013, *Monthly Notices of the Royal Astronomical Society*, 430, 1158
- Stott, J. P., Sobral, D., Swinbank, A. M., et al. 2014, *Monthly Notices of the Royal Astronomical Society*, 443, 2695
- Swinbank, A. M., Sobral, D., Smail, I. R., et al. 2012, *Monthly Notices of the Royal Astronomical Society*, 426, 935
- Tissera, P. B., Rosas-Guevara, Y., Bower, R. G., et al. 2018, eprint arXiv:1806.04575, 1806.04575
- Treu, T. L., Schmidt, K. B., Brammer, G. B., et al. 2015, *The Astrophysical Journal*, 812, 114
- van Dokkum, P. G., Brammer, G. B., Fumagalli, M., et al. 2011, *The Astrophysical Journal*, 743, L15
- Vogelsberger, M., Genel, S., Springel, V., et al. 2014, *Nature*, 509, 177
- Wang, X., Jones, T. A., Treu, T. L., et al. 2017, *The Astrophysical Journal*, 837, 89
- . 2019, *The Astrophysical Journal*, 882, 94
- Whitaker, K. E., Franx, M., Leja, J., et al. 2014, *The Astrophysical Journal*, 795, 104
- Wuyts, E., Wisnioski, E., Fossati, M., et al. 2016, *The Astrophysical Journal*, 827, 74
- Yuan, T., Kewley, L. J., & Rich, J. A. 2013, *The Astrophysical Journal*, 767, 106
- Zitrin, A., Fabris, A., Merten, J. C., et al. 2015, *The Astrophysical Journal*, 801, 44

Table 3. Measured quantities of our sample galaxies.

Cluster	ID	R.A. [deg.]	Dec. [deg.]	z_{spec}	$\Delta \log(\text{O}/\text{H})/\Delta r$ [dex/kpc]	Observed EL fluxes [$10^{-17} \text{ erg s}^{-1} \text{ cm}^{-2}$]						μC	Stellar continuum SED fitting				Nebular emission diagnostics									
						$f_{\text{[OII]}}$	$f_{\text{H}\gamma}$	$f_{\text{H}\beta}$	$f_{\text{[OIII]}}$	$f_{\text{H}\alpha}$	$f_{\text{[SII]}}$		$\log(M_* \mathcal{E}_{\text{[OII]}})$	$\text{SFR}^{\text{SED}}_{\text{[OII]}}$	A_V	ΔV	$12 + \log(\text{O}/\text{H})$	A_N	$\text{SFR}^{\text{NE}}_{\text{[OII]}}$							
A2744	00144	3.606322	-30.380061	1.34	0.020 ± 0.085	22.76	0.92	7.45 ± 2.39	2.28 ± 1.12	3.71 ± 3.10	6.38 ± 1.45	14.13 ± 1.17	1.08 ± 1.19	1.43 ^{+0.01} _{-0.01}	9.56 ^{+0.17} _{-0.17}	15.97 ^{+22.41} _{-22.41}	1.10 ^{+0.42} _{-0.42}	0.15 ^{+0.04} _{-0.04}	8.55 ^{+0.13} _{-0.22}	0.77 ^{+0.57} _{-0.45}	7.66 ^{+4.52} _{-4.45}	1.10 ^{+0.42} _{-0.42}	0.15 ^{+0.04} _{-0.04}	8.55 ^{+0.13} _{-0.22}	0.77 ^{+0.57} _{-0.45}	7.66 ^{+4.52} _{-4.45}
A2744	00161	3.588863	-30.380291	1.36	0.027 ± 0.063	23.55	0.93	4.50 ± 1.30	1.95 ± 0.65	2.71 ± 1.86	12.51 ± 1.21	6.31 ± 0.70	0.25 ± 0.71	2.12 ^{+0.02} _{-0.02}	8.53 ^{+0.18} _{-0.18}	2.72 ^{+5.94} _{-5.94}	0.40 ^{+0.32} _{-0.32}	0.05 ^{+0.01} _{-0.01}	8.00 ^{+0.21} _{-0.21}	< 0.27	1.88 ^{+0.65} _{-0.65}	0.40 ^{+0.32} _{-0.32}	0.05 ^{+0.01} _{-0.01}	8.00 ^{+0.21} _{-0.21}	< 0.27	1.88 ^{+0.65} _{-0.65}
A2744	00168	3.571780	-30.380437	1.68	-0.147 ± 0.079	23.83	0.58	4.45 ± 0.59	3.94 ± 1.00	3.07 ± 0.70	18.64 ± 0.74	2.76 ^{+0.02} _{-0.02}	8.11 ^{+0.05} _{-0.05}	0.40 ^{+0.01} _{-0.01}	0.40 ^{+0.01} _{-0.01}	8.06 ^{+0.25} _{-0.25}	< 1.06	< 14.87	0.40 ^{+0.01} _{-0.01}	0.40 ^{+0.01} _{-0.01}	8.06 ^{+0.25} _{-0.25}	< 1.06	< 14.87	
A2744	00189	3.573408	-30.380770	1.76	0.033 ± 0.030	21.77	0.95	16.97 ± 0.82	3.00 ± 1.43	5.48 ± 1.09	2.79 ^{+0.02} _{-0.02}	9.95 ^{+0.12} _{-0.12}	1.39 ^{+20.38} _{-1.39}	0.90 ^{+0.30} _{-0.30}	0.20 ^{+0.04} _{-0.04}	8.55 ^{+0.09} _{-0.09}	< 0.68	12.86 ^{+16.11} _{-16.11}	0.90 ^{+0.30} _{-0.30}	0.20 ^{+0.04} _{-0.04}	8.55 ^{+0.09} _{-0.09}	< 0.68	12.86 ^{+16.11} _{-16.11}
A2744	02623	3.591110	-30.381705	1.89	0.018 ± 0.014	23.02	0.65	6.68 ± 0.55	3.19 ± 0.84	4.14 ± 0.68	34.01 ± 0.75	2.21 ^{+0.02} _{-0.02}	8.38 ^{+0.12} _{-0.12}	10.39 ^{+4.87} _{-4.87}	0.20 ^{+0.11} _{-0.11}	0.05 ^{+0.00} _{-0.00}	8.02 ^{+0.10} _{-0.10}	0.90 ^{+0.62} _{-0.62}	21.64 ^{+10.71} _{-10.71}	0.20 ^{+0.11} _{-0.11}	0.05 ^{+0.00} _{-0.00}	8.02 ^{+0.10} _{-0.10}	0.90 ^{+0.62} _{-0.62}	21.64 ^{+10.71} _{-10.71}
A2744	08982	3.599948	-30.393554	1.34	0.044 ± 0.041	23.21	0.74	14.74 ± 0.98	3.14 ± 0.48	6.97 ± 0.45	37.56 ± 1.01	26.46 ± 0.54	5.58 ± 0.53	1.90 ^{+0.02} _{-0.02}	8.63 ^{+0.03} _{-0.03}	9.16 ^{+3.56} _{-3.56}	0.90 ^{+0.10} _{-0.10}	0.06 ^{+0.00} _{-0.00}	8.25 ^{+0.09} _{-0.09}	0.39 ^{+0.31} _{-0.31}	8.67 ^{+2.53} _{-2.53}	0.90 ^{+0.10} _{-0.10}	0.06 ^{+0.00} _{-0.00}	8.25 ^{+0.09} _{-0.09}	0.39 ^{+0.31} _{-0.31}	8.67 ^{+2.53} _{-2.53}
A2744	08983	3.600091	-30.393759	1.34	-0.066 ± 0.085	22.58	0.90	15.59 ± 1.46	1.02 ± 0.75	3.97 ± 0.67	17.64 ± 1.43	17.00 ± 0.79	4.91 ± 0.79	3.29 ^{+0.05} _{-0.05}	8.66 ^{+0.15} _{-0.15}	25.81 ^{+17.37} _{-17.37}	1.20 ^{+0.21} _{-0.21}	0.10 ^{+0.02} _{-0.02}	8.39 ^{+0.10} _{-0.10}	< 0.38	5.33 ^{+1.83} _{-1.83}	1.20 ^{+0.21} _{-0.21}	0.10 ^{+0.02} _{-0.02}	8.39 ^{+0.10} _{-0.10}	< 0.38	5.33 ^{+1.83} _{-1.83}
A2744	08985	3.576755	-30.393627	1.37	0.139 ± 0.079	22.91	0.87	14.76 ± 1.07	0.05 ± 0.64	6.59 ± 0.91	22.15 ± 1.11	18.12 ± 0.64	2.56 ± 0.64	3.29 ^{+0.04} _{-0.04}	8.66 ^{+0.15} _{-0.15}	3.11 ^{+9.15} _{-9.15}	0.70 ^{+0.26} _{-0.26}	0.06 ^{+0.00} _{-0.00}	8.29 ^{+0.09} _{-0.09}	1.41 ^{+0.31} _{-0.31}	7.81 ^{+2.54} _{-2.54}	0.70 ^{+0.26} _{-0.26}	0.06 ^{+0.00} _{-0.00}	8.29 ^{+0.09} _{-0.09}	1.41 ^{+0.31} _{-0.31}	7.81 ^{+2.54} _{-2.54}
A2744	08985	3.576755	-30.393627	1.37	0.139 ± 0.079	22.91	0.87	14.76 ± 1.07	0.05 ± 0.64	6.59 ± 0.91	22.15 ± 1.11	18.12 ± 0.64	2.56 ± 0.64	3.29 ^{+0.04} _{-0.04}	8.66 ^{+0.15} _{-0.15}	3.11 ^{+9.15} _{-9.15}	0.70 ^{+0.26} _{-0.26}	0.06 ^{+0.00} _{-0.00}	8.29 ^{+0.09} _{-0.09}	1.41 ^{+0.31} _{-0.31}	7.81 ^{+2.54} _{-2.54}	0.70 ^{+0.26} _{-0.26}	0.06 ^{+0.00} _{-0.00}	8.29 ^{+0.09} _{-0.09}	1.41 ^{+0.31} _{-0.31}	7.81 ^{+2.54} _{-2.54}
A2744	08985	3.576755	-30.393627	1.37	0.139 ± 0.079	22.91	0.87	14.76 ± 1.07	0.05 ± 0.64	6.59 ± 0.91	22.15 ± 1.11	18.12 ± 0.64	2.56 ± 0.64	3.29 ^{+0.04} _{-0.04}	8.66 ^{+0.15} _{-0.15}	3.11 ^{+9.15} _{-9.15}	0.70 ^{+0.26} _{-0.26}	0.06 ^{+0.00} _{-0.00}	8.29 ^{+0.09} _{-0.09}	1.41 ^{+0.31} _{-0.31}	7.81 ^{+2.54} _{-2.54}	0.70 ^{+0.26} _{-0.26}	0.06 ^{+0.00} _{-0.00}	8.29 ^{+0.09} _{-0.09}	1.41 ^{+0.31} _{-0.31}	7.81 ^{+2.54} _{-2.54}
A2744	08985	3.576755	-30.393627	1.37	0.139 ± 0.079	22.91	0.87	14.76 ± 1.07	0.05 ± 0.64	6.59 ± 0.91	22.15 ± 1.11	18.12 ± 0.64	2.56 ± 0.64	3.29 ^{+0.04} _{-0.04}	8.66 ^{+0.15} _{-0.15}	3.11 ^{+9.15} _{-9.15}	0.70 ^{+0.26} _{-0.26}	0.06 ^{+0.00} _{-0.00}	8.29 ^{+0.09} _{-0.09}	1.41 ^{+0.31} _{-0.31}	7.81 ^{+2.54} _{-2.54}	0.70 ^{+0.26} _{-0.26}	0.06 ^{+0.00} _{-0.00}	8.29 ^{+0.09} _{-0.09}	1.41 ^{+0.31} _{-0.31}	7.81 ^{+2.54} _{-2.54}
A2744	08985	3.576755	-30.393627	1.37	0.139 ± 0.079	22.91	0.87	14.76 ± 1.07	0.05 ± 0.64	6.59 ± 0.91	22.15 ± 1.11	18.12 ± 0.64	2.56 ± 0.64	3.29 ^{+0.04} _{-0.04}	8.66 ^{+0.15} _{-0.15}	3.11 ^{+9.15} _{-9.15}	0.70 ^{+0.26} _{-0.26}	0.06 ^{+0.00} _{-0.00}	8.29 ^{+0.09} _{-0.09}	1.41 ^{+0.31} _{-0.31}	7.81 ^{+2.54} _{-2.54}	0.70 ^{+0.26} _{-0.26}	0.06 ^{+0.00} _{-0.00}	8.29 ^{+0.09} _{-0.09}	1.41 ^{+0.31} _{-0.31}	7.81 ^{+2.54} _{-2.54}
A2744	08985	3.576755	-30.393627	1.37	0.139 ± 0.079	22.91	0.87	14.76 ± 1.07	0.05 ± 0.64	6.59 ± 0.91	22.15 ± 1.11	18.12 ± 0.64	2.56 ± 0.64	3.29 ^{+0.04} _{-0.04}	8.66 ^{+0.15} _{-0.15}	3.11 ^{+9.15} _{-9.15}	0.70 ^{+0.26} _{-0.26}	0.06 ^{+0.00} _{-0.00}	8.29 ^{+0.09} _{-0.09}	1.41 ^{+0.31} _{-0.31}	7.81 ^{+2.54} _{-2.54}	0.70 ^{+0.26} _{-0.26}	0.06 ^{+0.00} _{-0.00}	8.29 ^{+0.09} _{-0.09}	1.41 ^{+0.31} _{-0.31}	7.81 ^{+2.54} _{-2.54}
A2744	08985	3.576755	-30.393627	1.37	0.139 ± 0.079	22.91	0.87	14.76 ± 1.07	0.05 ± 0.64	6.59 ± 0.91	22.15 ± 1.11	18.12 ± 0.64	2.56 ± 0.64	3.29 ^{+0.04} _{-0.04}	8.66 ^{+0.15} _{-0.15}	3.11 ^{+9.15} _{-9.15}	0.70 ^{+0.26} _{-0.26}	0.06 ^{+0.00} _{-0.00}	8.29 ^{+0.09} _{-0.09}	1.41 ^{+0.31} _{-0.31}	7.81 ^{+2.54} _{-2.54}	0.70 ^{+0.26} _{-0.26}	0.06 ^{+0.00} _{-0.00}	8.29 ^{+0.09} _{-0.09}	1.41 ^{+0.31} _{-0.31}	7.81 ^{+2.54} _{-2.54}
A2744	08985	3.576755	-30.393627	1.37	0.139 ± 0.079	22.91	0.87	14.76 ± 1.07	0.05 ± 0.64	6.59 ± 0.91	22.15 ± 1.11	18.12 ± 0.64	2.56 ± 0.64	3.29 ^{+0.04} _{-0.04}	8.66 ^{+0.15} _{-0.15}	3.11 ^{+9.15} _{-9.15}	0.70 ^{+0.26} _{-0.26}	0.06 ^{+0.00} _{-0.00}	8.29 ^{+0.09} _{-0.09}	1.41 ^{+0.31} _{-0.31}	7.81 ^{+2.54} _{-2.54}	0.70 ^{+0.26} _{-0.26}	0.06 ^{+0.00} _{-0.00}	8.29 ^{+0.09} _{-0.09}	1.41 ^{+0.31} _{-0.31}	7.81 ^{+2.54} _{-2.54}
A2744	08985	3.576755	-30.393627	1.37	0.139 ± 0.079	22.91	0.87	14.76 ± 1.07	0.05 ± 0.64	6.59 ± 0.91	22.15 ± 1.11	18.12 ± 0.64	2.56 ± 0.64	3.29 ^{+0.04} _{-0.04}	8.66 ^{+0.15} _{-0.15}	3.11 ^{+9.15} _{-9.15}	0.70 ^{+0.26} _{-0.26}	0.06 ^{+0.00} _{-0.00}	8.29 ^{+0.09} _{-0.09}	1.41 ^{+0.31} _{-0.31}	7.81 ^{+2.54} _{-2.54}	0.70 ^{+0.26} _{-0.26}	0.06 ^{+0.00} _{-0.00}	8.29 ^{+0.09} _{-0.09}	1.41 ^{+0.31} _{-0.31}	7.81 ^{+2.54} _{-2.54}
A2744	08985	3.576755	-30.393627	1.37	0.139 ± 0.079	22.91	0.87	14.76 ± 1.07	0.05 ± 0.64	6.59 ± 0.91	22.15 ± 1.11	18.12 ± 0.64	2.56 ± 0.64	3.29 ^{+0.04} _{-0.04}	8.66 ^{+0.15} _{-0.15}	3.11 ^{+9.15} _{-9.15}	0.70 ^{+0.26} _{-0.26}	0.06 ^{+0.00} _{-0.00}	8.29 ^{+0.09} _{-0.09}	1.41 ^{+0.31} _{-0.31}	7.81 ^{+2.54} _{-2.54}	0.70 ^{+0.26} _{-0.26}	0.06 ^{+0.00} _{-0.00}	8.29 ^{+0.09} _{-0.09}	1.41 ^{+0.31} _{-0.31}	7.81 ^{+2.54} _{-2.54}
A2744	08985	3.576755	-30.393627	1.37	0.139 ± 0.079	22.91	0.87	14.76 ± 1.07	0.05 ± 0.64	6.59 ± 0.91	22.15 ± 1.11	18.12 ± 0.64	2.56 ± 0.64	3.29 ^{+0.04} _{-0.04}	8.66 ^{+0.15} _{-0.15}	3.11 ^{+9.15} _{-9.15}	0.70 ^{+0.26} _{-0.26}	0.06 ^{+0.00} _{-0.00}	8.29 ^{+0.09} _{-0.09}	1.41 ^{+0.31} _{-0.31}	7.81 ^{+2.54} _{-2.54}	0.70 ^{+0.26} _{-0.26}	0.06 ^{+0.00} _{-0.00}	8.29 ^{+0.09} _{-0.09}	1.41 ^{+0.31} _{-0.31}	7.81 ^{+2.54} _{-2.54}
A2744	08985	3.576755	-30.393627	1.37	0.139 ± 0.079	22.91	0.87	14.76 ± 1.07	0.05 ± 0.64	6.59 ± 0.91	22.15 ± 1.11	18.12 ± 0.64	2.56 ± 0.64	3.29 ^{+0.04} _{-0.04}	8.66 ^{+0.15} _{-0.15}	3.11 ^{+9.15} _{-9.15}	0.70 ^{+0.26} _{-0.26}	0.06 ^{+0.00} _{-0.00}	8.29 ^{+0.09} _{-0.09}	1.41 ^{+0.31} _{-0.31}	7.81 ^{+2.54} _{-2.54}	0.70 ^{+0.26} _{-0.26}	0.06 ^{+0.00} _{-0.00}	8.29 ^{+0.09} _{-0.09}	1.41 ^{+0.31} _{-0.31}	7.81 ^{+2.54} _{-2.54}
A2744	08985	3.576755	-30.393627	1.37	0.139 ± 0.079	22.91	0.8																			

Table 3 (continued)

Cluster	ID	R.A. [deg.]	Dec. [deg.]	z_{spec}	$\Delta \log(\text{O}/\text{H})/\Delta r$ [dex/kpc]	b_{F140W} [ÅBmag]	Observed EL fluxes [$10^{-17} \text{ erg s}^{-1} \text{ cm}^{-2}$]					μC	Stellar continuum SED fitting			[N II]/H α d	Nebular emission diagnostics				
							$f_{[\text{OII}]}$	$f_{\text{H}\gamma}$	$f_{\text{H}\beta}$	$f_{[\text{OIII}]}$	$f_{\text{H}\alpha}$		$f_{[\text{SII}]}$	$\log(M_*, \mathcal{E}_{M_0})$	SFR \mathcal{E} [M_{\odot}/yr]		A^S	A^N	$12 + \log(\text{O}/\text{H})$	SFR \mathcal{N} [M_{\odot}/yr]	
M1423	00430	215.944735	24.088841	1.79	0.104 \pm 0.054	23.19	0.77	7.50 \pm 0.47	3.10 \pm 0.71	3.08 \pm 0.54	18.78 \pm 0.64	1.46 \pm 0.02	9.03 \pm 0.17	10.22 \pm 18.14	0.60 \pm 0.11	0.08 \pm 0.01	8.24 \pm 0.12	< 0.59	15.47 \pm 25.95
M1423	00433	215.954478	24.088107	1.63	-0.095 \pm 0.046	23.00	0.80	7.83 \pm 0.85	0.47 \pm 0.61	4.28 \pm 1.70	18.45 \pm 1.03	3.64 \pm 0.06	8.94 \pm 0.15	10.22 \pm 8.63	1.00 \pm 0.28	0.08 \pm 0.01	8.27 \pm 0.15	< 1.03	8.97 \pm 20.72
M1423	00493	215.952044	24.083337	1.78	-0.028 \pm 0.089	21.75	0.93	13.40 \pm 2.17	3.05 \pm 3.47	19.79 \pm 2.00	18.92 \pm 2.61	5.14 \pm 0.42	9.66 \pm 0.24	6.00 \pm 9.50	0.60 \pm 0.44	0.14 \pm 0.05	8.52 \pm 0.13	1.67 \pm 0.39	> 26.26
M1423	00908	215.957460	24.079767	1.31	-0.233 \pm 0.104	21.91	0.96	12.88 \pm 4.10	...	4.07 \pm 2.50	8.01 \pm 3.07	17.25 \pm 1.47	...	2.12 \pm 0.03	9.54 \pm 0.12	12.11 \pm 78.23	1.20 \pm 0.51	0.15 \pm 0.09	8.60 \pm 0.17	0.75 \pm 0.75	5.81 \pm 4.91
M1423	00909	215.957063	24.079622	1.32	-0.260 \pm 0.085	23.08	0.86	16.21 \pm 1.76	3.73 \pm 0.82	3.47 \pm 1.24	12.18 \pm 1.48	14.55 \pm 0.78	4.38 \pm 0.78	2.21 \pm 0.01	8.72 \pm 0.12	6.09 \pm 5.65	0.60 \pm 0.26	0.06 \pm 0.01	8.51 \pm 0.08	< 0.28	3.66 \pm 1.09
M1423	00976	215.938230	24.078815	1.24	-0.023 \pm 0.059	22.85	0.89	9.56 \pm 1.47	1.96 \pm 0.60	4.02 \pm 0.46	17.47 \pm 0.53	15.17 \pm 0.57	2.78 \pm 0.55	1.45 \pm 0.01	9.00 \pm 0.17	3.54 \pm 22.83	0.50 \pm 0.50	0.09 \pm 0.01	8.30 \pm 0.09	0.44 \pm 0.29	5.49 \pm 1.61
M1423	01682	215.943034	24.069804	1.32	-0.000 \pm 0.038	23.80	0.90	8.07 \pm 1.04	1.59 \pm 0.47	4.30 \pm 1.63	17.49 \pm 0.89	6.85 \pm 0.47	1.67 \pm 0.48	2.85 \pm 0.07	8.68 \pm 0.01	0.02 \pm 0.24	0.60 \pm 0.12	0.06 \pm 0.00	8.33 \pm 0.10	< 0.22	1.53 \pm 0.48
M1423	01808	215.960238	24.065007	2.02	0.035 \pm 0.053	23.33	0.87	4.28 \pm 0.36	0.90 \pm 0.52	1.92 \pm 0.79	8.75 \pm 0.54	1.28 \pm 0.01	9.44 \pm 0.13	14.51 \pm 12.61	0.60 \pm 0.20	0.11 \pm 0.01	8.33 \pm 0.13	1.04 \pm 1.08	21.46 \pm 56.60
M2129	00340	322.352173	-7.679022	2.09	-0.021 \pm 0.018	23.73	0.81	1.95 \pm 0.89	1.08 \pm 0.64	0.64 \pm 0.57	10.54 \pm 0.65	1.46 \pm 0.02	8.94 \pm 0.17	20.70 \pm 13.92	0.07 \pm 0.00	0.00 \pm 0.00	7.84 \pm 0.40	1.75 \pm 1.18	43.84 \pm 31.88
M2129	00380	322.364762	-7.679957	1.81	-0.064 \pm 0.032	24.55	0.67	1.50 \pm 0.39	2.06 \pm 0.58	2.22 \pm 0.77	6.94 \pm 0.54	1.56 \pm 0.02	8.23 \pm 0.17	3.94 \pm 1.05	0.40 \pm 0.11	0.05 \pm 0.00	7.89 \pm 0.41	1.47 \pm 1.36	16.98 \pm 56.16
M2129	00411	322.353278	-7.680522	1.24	-0.001 \pm 0.047	22.67	0.97	2.61 \pm 1.85	1.01 \pm 0.70	1.43 \pm 0.49	4.17 \pm 0.58	5.14 \pm 0.66	1.10 \pm 0.65	1.39 \pm 0.01	9.54 \pm 0.07	0.55 \pm 5.09	0.90 \pm 0.24	0.16 \pm 0.01	8.27 \pm 0.18	0.93 \pm 0.99	2.65 \pm 3.24
M2129	00440	322.366118	-7.681231	1.36	0.034 \pm 0.050	22.16	0.88	8.43 \pm 1.81	...	6.34 \pm 2.65	8.86 \pm 1.97	33.17 \pm 1.40	6.90 \pm 1.34	1.53 \pm 0.02	9.63 \pm 0.13	59.37 \pm 56.40	1.50 \pm 0.22	0.16 \pm 0.03	8.63 \pm 0.12	2.05 \pm 0.42	44.89 \pm 17.40
M2129	00465	322.367391	-7.681865	1.36	0.036 \pm 0.027	22.34	0.88	7.06 \pm 1.23	1.81 \pm 0.62	3.08 \pm 0.85	1.27 \pm 1.15	27.21 \pm 0.70	5.59 \pm 0.68	1.57 \pm 0.02	9.71 \pm 0.08	2.92 \pm 99.02	1.20 \pm 0.80	0.18 \pm 0.02	8.90 \pm 0.13	2.26 \pm 0.58	42.01 \pm 24.05
M2129	00565	322.364752	-7.683770	1.37	0.064 \pm 0.064	22.34	0.92	10.16 \pm 2.04	1.77 \pm 1.00	12.87 \pm 2.50	15.41 \pm 1.84	17.05 \pm 1.14	5.64 \pm 1.14	2.00 \pm 0.02	9.46 \pm 0.16	1.65 \pm 1.19	0.70 \pm 0.27	0.13 \pm 0.02	8.33 \pm 0.15	< 0.42	5.60 \pm 1.34
M2129	00690	322.346464	-7.685883	1.88	0.049 \pm 0.043	23.08	0.78	9.45 \pm 0.59	0.70 \pm 0.95	4.85 \pm 0.76	18.93 \pm 0.82	2.73 \pm 0.07	8.88 \pm 0.10	15.05 \pm 6.52	0.80 \pm 0.10	0.06 \pm 0.00	8.33 \pm 0.14	< 1.01	15.12 \pm 27.89
M2129	01408	322.369038	-7.700541	1.48	0.087 \pm 0.125	23.65	0.83	4.86 \pm 0.70	1.39 \pm 0.45	2.27 \pm 0.73	8.91 \pm 0.79	8.43 \pm 0.57	4.23 \pm 0.76	1.49 \pm 0.02	8.98 \pm 0.16	16.52 \pm 9.96	1.20 \pm 0.21	0.08 \pm 0.01	8.32 \pm 0.15	< 0.48	4.81 \pm 2.41
M2129	01539	322.363350	-7.703212	1.64	0.021 \pm 0.027	22.08	0.94	13.52 \pm 0.95	0.45 \pm 1.21	6.47 \pm 1.12	9.61 \pm 1.12	1.39 \pm 0.01	9.31 \pm 0.11	6.99 \pm 7.03	0.50 \pm 0.36	0.11 \pm 0.01	8.63 \pm 0.13	1.09 \pm 0.75	31.57 \pm 55.80
M2129	01665	322.358149	-7.706707	1.56	-0.028 \pm 0.030	23.26	0.79	6.84 \pm 0.68	1.91 \pm 0.47	3.74 \pm 0.78	15.71 \pm 0.85	4.35 \pm 1.29	...	1.27 \pm 0.01	9.76 \pm 0.05	15.01 \pm 36.90	1.00 \pm 0.00	0.14 \pm 0.00	8.24 \pm 0.13	< 0.28	6.23 \pm 2.77
RXJ1347	00664	206.904786	-11.750602	1.69	-0.087 \pm 0.040	23.01	0.48	12.64 \pm 0.65	4.88 \pm 1.09	5.93 \pm 0.79	51.74 \pm 0.95	1.40 \pm 0.07	9.49 \pm 0.19	0.77 \pm 46.86	0.30 \pm 0.62	0.12 \pm 0.03	8.53 \pm 0.10	< 0.85	34.43 \pm 54.74
RXJ1347	01443	206.882540	-11.764358	1.77	-0.028 \pm 0.038	21.75	0.93	21.20 \pm 0.96	...	6.34 \pm 1.21	18.50 \pm 1.30	1.83 \pm 0.01	9.87 \pm 0.09	0.05 \pm 0.05	0.50 \pm 0.20	0.22 \pm 0.01	8.60 \pm 0.11	< 0.23	4.09 \pm 0.73
RXJ2248	00206	342.175906	-44.516503	1.43	-0.020 \pm 0.104	21.53	0.97	14.31 \pm 1.82	0.36 \pm 1.05	7.84 \pm 1.80	7.13 \pm 1.72	12.87 \pm 1.05	...	1.83 \pm 0.01	9.87 \pm 0.09	0.05 \pm 0.05	0.50 \pm 0.20	0.22 \pm 0.01	8.60 \pm 0.11	< 0.23	4.09 \pm 0.73
RXJ2248	00428	342.186462	-44.521187	1.23	0.052 \pm 0.036	22.19	0.96	8.61 \pm 5.13	0.95 \pm 1.51	10.12 \pm 1.11	24.10 \pm 1.15	11.30 \pm 1.33	...	4.97 \pm 0.08	9.13 \pm 0.15	1.92 \pm 0.32	0.20 \pm 0.11	0.10 \pm 0.00	8.05 \pm 0.24	< 0.19	1.31 \pm 0.25
RXJ2248	00786	342.169402	-44.527222	1.84	-0.135 \pm 0.070	23.81	0.46	7.24 \pm 0.67	2.04 \pm 0.97	2.77 \pm 0.76	25.73 \pm 0.86	3.38 \pm 0.06	7.96 \pm 0.03	2.70 \pm 0.05	0.30 \pm 0.00	0.05 \pm 0.00	8.12 \pm 0.13	< 0.73	9.32 \pm 15.70
RXJ2248	01250	342.192946	-44.536578	1.40	-0.068 \pm 0.094	22.52	0.88	8.96 \pm 2.06	...	0.25 \pm 2.06	15.49 \pm 1.92	17.06 \pm 1.11	4.18 \pm 1.13	3.14 \pm 0.04	9.17 \pm 0.08	0.16 \pm 1.02	0.20 \pm 0.33	0.09 \pm 0.01	8.41 \pm 0.12	1.14 \pm 0.62	6.71 \pm 4.51
M1149	00270	177.385990	22.414074	1.27	-0.160 \pm 0.030	22.55	0.71	10.28 \pm 5.23	4.84 \pm 8.65	24.87 \pm 0.94	29.58 \pm 0.72	13.33 \pm 0.36	0.36 \pm 0.35	1.96 \pm 0.03	9.00 \pm 0.04	0.24 \pm 13.16	0.20 \pm 0.20	0.09 \pm 0.00	7.91 \pm 0.15	< 0.03	3.04 \pm 0.15
M1149	00593	177.406922	22.407499	1.48	-0.010 \pm 0.020	22.40	0.81	23.44 \pm 1.40	6.00 \pm 0.85	5.72 \pm 0.44	31.48 \pm 0.45	29.90 \pm 0.34	5.31 \pm 0.41	2.02 \pm 0.03	9.13 \pm 0.09	39.40 \pm 0.65	1.00 \pm 0.03	0.09 \pm 0.01	8.38 \pm 0.06	0.93 \pm 0.14	17.50 \pm 2.32
M1149	06000	177.389220	22.407583	2.31	-0.180 \pm 0.080	24.12	0.76	1.01 \pm 0.38	1.33 \pm 0.29	1.40 \pm 0.27	8.31 \pm 0.31	6.87 \pm 0.03	8.32 \pm 0.03	0.90 \pm 0.04	0.00 \pm 0.00	0.04 \pm 0.00	7.83 \pm 0.23	< 0.85	3.10 \pm 6.58
M1149	06076	177.415126	22.406195	1.68	0.060 \pm 0.050	23.31	0.7														

Table 3 (*continued*)

Cluster	ID	R.A. [deg.]	Dec. [deg.]	z_{spec}	$\Delta \log(\text{O}/\text{H})/\Delta r$ [dex/kpc]	F_{F140W}^a [ABmag]	Observed EL fluxes [$10^{-17} \text{ erg s}^{-1} \text{ cm}^{-2}$]					μC	Stellar continuum SED fitting			Nebular emission diagnostics		
							$f_{\text{[OII]}}$	$f_{\text{H}\gamma}$	$f_{\text{H}\beta}$	$f_{\text{[OIII]}}$	$f_{\text{H}\alpha}$		$f_{\text{[SII]}}$	$\log(M_\star)$	$e_{(M_\odot)}$	$\text{SFR}^{\text{SED}}_{(M_\odot/\text{yr})}$	A_V^{S}	$12 + \log(\text{O}/\text{H})$

^a The observed H_{140} -band magnitude, before accounting for lensing magnification.

^b The reduction factor of H_{140} -band flux, after subtracting the nebular emission that falls within the corresponding wavelength window.

^c The lensing magnification estimated from various mass models of galaxy clusters. For all the *HFF* clusters, we use the SHARPS & JOHANSSON version 4corr models (Johnson et al. 2014). For all the *CLASH*-only clusters except RXJ1347, we use the Zitrin PIEMD+eNFW version 2 models (Zitrin et al. 2015). For RXJ1347, we use our own model built following closely the approach in Johnson et al. (2014).

^d The flux ratio of [N II] and H α , estimated from the prescription of Faist et al. (2017). This value is used to correct for the blended H α -[N II] fluxes in grism spectra, if necessary.

^e Values presented here are corrected for lensing magnification.